

THE FLORIDA STATE UNIVERSITY
COLLEGE OF ARTS AND SCIENCES

THE INFLUENCE OF THE ALASKAN GYRE ON THE COASTAL
CIRCULATION IN THE GULF OF ALASKA

By

PAUL K. HEIM II

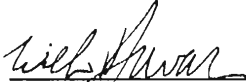
A Thesis submitted to the
Department of Oceanography
in partial fulfillment of the requirements
for the degree of Master of Science

Degree Awarded:
Summer Semester, 1991


The members of the Committee approve the thesis of Paul K. Heim II, defended on April 19, 1991.



James J. O'Brien
Professor Directing Thesis




William K. Dewar
Committee Member

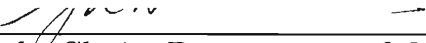


Richard L. Iverson
Committee Member

Approved:



Ya Hsueh, Chair, Department of Oceanography



Ya Hsueh, Chair, Department of Oceanography

DA STATE

460

LD

HEIM II
27. 13

1991

è Donna and our son Brian

LR5 86

10 452TF 24 950 TH
91

4354

Acknowledgement

This work was supported by The Office of Naval Research, NASA Oceanic Processes, and the National Science Foundation under grant OCE-88111316. Computer time was supplied by The Florida State University's Cray Y-MP.

I wish to express my deepest gratitude to Dr. James J. O'Brien, my major professor and thesis advisor. His advice, motivation and support throughout my tenure at Florida State University are greatly appreciated. I also wish to thank Dr. William K. Dewar and Dr. Richard L. Iverson for taking the time to serve on my committee.

I cannot thank my wife and family enough for their unconditional love and support throughout this endeavor.

I want to thank Dr. Ben Cagle for inspiring me to apply for admission to FSU Master's program. I want to thank my colleagues at the Mesoscale Air-Sea interaction Group for their friendship and constructive comments and suggestions. In particular I would like to thank Dr. Mark Johnson, his help and advice were instrumental in the completion of this work. Thanks to Mr. Steve Gill at NOS who supplied much needed sea level data and to Dr. Harley Hurlburt and Mr. Joe Metzger, both from NOARL for supplying me with some of their model results. Additionally I would like to thank Mr. Alan Davis for all of his computer and technical assistance.

assistance.

Table of Contents

	Page
Acknowledgement	iv
List of Tables	vii
List of Figures	viii
Abstract	xv
1. Introduction	1
2. NE Pacific Circulation Overview	4
2.1 The Alaskan Stream.....	4
2.2 The Alaska Coastal Current.....	12
2.3 The Sitka Eddy	14
2.4 General Bathymetry of the Region	17
2.5 Climatology	18
3. The Model	21
3.1 Background.....	21
3.2 Equations	21
3.3 Boundary Conditions	28
3.4 Bottom Topography.....	29
4. Forcing	32
4.1 COADS Winds.....	32
4.2 EOF Method	37
4.1 COADS Winds.....	32
4.2 EOF Method.....	37
4.3 EOF Analysis.....	40

5.	Results	55
	5.1 Model Features	55
	5.2 Model Validation.....	66
6.	Conclusions	77
7.	References	79
8.	Biographical Sketch	83

List of Tables

	Page
Table 1 Values of parameters used in the model.....	25
Table 2 Percent and cumulative percent variance for the first nine eigenvectors computed from the curl of the COADS pseudo wind stress data from 1970 through 1989. Over 40% of the total variance is accounted for by the first three modes. The higher modes are attributed to noise	41

List of Figures

	Page
Figure 1: Major surface currents of the North Pacific Ocean (from <i>Tabata</i> , 1976). The major currents of the NE Pacific region include the Subarctic Current, the Alaska Current, and the Alaskan Stream.....	5
Figure 2: Schematic diagram of the surface circulation for the northwest Gulf of Alaska showing the Alaska Coastal Current in relation to the Alaska Current near Kodiak Island (from <i>Royer et al.</i> , 1990). The relatively dilute ACC hugs the shoreline while the Alaska Current remains on the continental slope. Current velocities are similar, but the transport of the ACC is an order of magnitude less than that of the Alaska Current.....	13
Figure 3: Geopotential anomaly at the sea surface relative to the 1000 db surface in the northeast Pacific during March-April 1958 (from <i>Tabata</i> , 1982). The Sitka eddy is centered at 57° N 140°W. The size of the Sitka eddy is greater than the feature generated by the model. The reader should notice that there is no data southwest of the eddy center.....	15
Figure 4: Bottom topography chart for the NE Pacific Ocean region. The general area of the Sitka eddy is indicated by the dotted square (from <i>Tabata</i> [1982]).....	19
Figure 5: Typical geometry for a reduced gravity model. Only the top layer is dynamically active	22
Figure 6: This figure shows the NE Pacific Ocean model region with the model domain outlined by the dashed line. Sea level from selected stations (Neah Bay, Sitka, and Kodiak) is used for model validation. The coastal outline is from the NCAR graphics data base.....	23

Figure 7: Staggered Arakawa C-grid used in the finite difference discretization of the governing equations, showing the relative locations of U, V, and H..... 27

Figure 8: Coastal geometry superimposed on model land boundaries (shaded region) with labelled bathymetry contours. Model land boundaries were defined by the 10 meter isobath with some local adjustments so that the local boundaries look reasonable. It is important to point out that the shallow bank east of Queen Charlotte Island is treated as a solid boundary by the model..... 31

Figure 9: Twenty year time series plot of COADS pseudo wind stress near 58°N, 146°W. Maxima (minima) normally occurring during winter (summer) months. Note the largest maximum occurs in February 1989, and that the maxima trend is increasing 33

Figure 10a-c: Sample wind stress vectors for (a) January '87, (b) July '87, (c) October '87. Note that the magnitude and direction of the wind stress changes dramatically from summer to winter. During January, the winds in the central basin are northward, turning eastward and weakening considerably by July. By October, the winds strengthen again and begin veering back to the north. Note particularly during October the divergence of the winds near 46° N, 136° W where the current also separates to form the Alaska and California Currents 35

Figure 11: Power spectrum (in variance preserving plot) for the time series shown in Figure 9. The data were smoothed in time with one Hanning pass prior to spectral computation. The winds are clearly dominated by the annual period, with no significant energy present at the "storm band" frequencies (4-10 days). There is additional energy at six and 24 months, evidence of semi-annual and interannual variability of the data 36

..... of semi-annual and interannual variability of the data 36

Figure 12: Twenty year temporal mean COADS wind stress curl pattern. Positive values are marked by solid lines, negative values by dashed lines. Maxima are marked with an

"H", minima with an "L". The large positive (cyclonic) curl in the northwest corner is probably the mean position of the Aleutian Low. The negative contours (anticyclonic) in the southern portion of the figure are evidence of the subtropical high..... 42

Figure 13a: Contour plot of the spatial pattern for EOF mode one. The high contour in the southwest corner reflects the annual southward migration of the Aleutian Low. The other high contour near 55° N, 136° W is believed to be caused by a low pressure system frequently located there. The diagonal band of negative curl influences the model results forcing an annual signal along the coast 46

Figure 13b-c: (b) Twenty year time series of EOF mode one with the 12 month running mean superimposed showing the interannual variability. Maxima (minima) normally occurring during winter (summer) months. (c) Detailed plot of the four years of pseudo stress used to force the model. The spatial pattern in Fig. 13a is multiplied by this time series. There is an intensification of the spatial pattern for large positive peaks, little change when the time series is near unity, and the opposite pattern (positive and negative contours reversed) for large negative peaks..... 47

Figure 13d: Power spectrum of EOF mode one. The abscissa units for $\log_{10}(\text{frequency})$ in this and all spectra plots in this section is months^{-1} , and the ordinate units are energy multiplied by frequency. This plot shows that the annual period (spike at -1.1) dominates. There also is some energy at the semi-annual (spike at -0.75) and interannual periods (spike at -1.25). Thus the variations in the spatial pattern in Fig 13a occur predominantly over periods of one year..... 48

Figure 14a: Contour plot of the spatial pattern for EOF mode two. The negative contours in the lower portion indicate that the intensity of the subtropical high is increased (decreased) when the time series in Fig. 14b is positive (negative). Likewise, the "H" contour in the mean representative of the the intensity of the subtropical high is increased (decreased) when the time series in Fig. 14b is positive (negative). Likewise, the "H" contour in the mean representative of the Aleutian Low is weakened (intensified) and moved northwestward (southeastward) when the time series is positive (negative). This interpretation is supported by

climatology. The diagonal band of low contours seen in Fig. 13a is also seen here, but at a much smaller amplitude. The high near 55° N, 136° W in mode one is also present in mode two, but is larger and shifted to the east. The power spectrum for this mode indicates that this pattern's primary period of oscillation is six months..... 49

Figure 14b: Time series plot of EOF mode two. The spatial pattern in Fig. 14a is multiplied by this time series, causing intensification for large positive peaks, little change when the time series is near unity, and creating the opposite pattern (positive and negative contours reversed) for large negative peaks 50

Figure 14c: Power spectrum of EOF mode two. This mode is dominated by the semi-annual period (spike at -0.78) with additional energy at periods of nine months and one year..... 51

Figure 15a: Contour plot of the spatial pattern for EOF mode three. Patterns and their oscillations are similar to those described in modes one and two..... 52

Figure 15b: Time series plot of EOF mode three. The results of the multiplication of the spatial pattern in Fig. 15a with this time series is the same as it was for the previous two modes..... 53

Figure 15c: Power spectrum of EOF mode three. All of the energy is contained in the annual signal..... 54

Figure 16a-c: Model domain super imposed with a five degree resolution grid (a), a one degree resolution grid(b), and a 1/3 degree resolution grid(c)..... 56

Figure 17: Model solution for 15 JAN 88. The arrows represent surface velocity vectors whose length is proportional to speed which is scaled in relation to the one cm/sec vector in the lower right hand corner. The cross isopycnal flows represent surface velocity vectors whose length is proportional to speed which is scaled in relation to the one cm/sec vector in the lower right hand corner. The cross isopycnal flows marked by very small velocity vectors are extremely weak but nevertheless show ageostrophic flow. The colors represent model upper layer thickness (ULT) or depth to the thermocline

(in meters) which is an analog of sea surface height. The color bar shows that the reds represent deep ULT (high sea surface height/downwelling region) and the blues represent shallow ULT (low sea surface height/upwelling region). The Alaskan Gyre is seen in the upper left hand portion of the domain color contoured from cyan to purple. The eastward flowing Subarctic Current in the southern portion of the figure splits as it impinges on the continental boundary. It flows northward as the Alaska Current and following the coastal geometry bends westward until it flows southwestward past Kodiak Island. The Alaska Current splits near 145° W and a portion of the current hugs the coast similar to the ACC, while the remainder of the current continues flowing west. South of Kodiak the Alaska Current narrows and intensifies forming into the Alaskan Stream. This demonstrates the ability of the model to simulate the Alaskan Gyre, bifurcation regions, and eastern and western boundary currents as well..... 58

Figure 18a-d: These figures show the annual cycle of the model results. Figure 18a shows the high coastal sea level (thin red band) beginning to form in November near 53° N. The red band increases in magnitude (thickness) and reaches its northern extent (near Kodiak island) by February 1988 (Fig. 18b). The decrease in coastal sea level occurs in the spring, beginning in the southeast and continues to decrease throughout the summer. By mid June, the southern extent of the high sea level signal has moved north from 50° N to north of Queen Charlotte Island (Figure 18c). This trend continues throughout the summer so that by early fall the sea level is lowest all along the coast (Figure 18d). Also notice the red blocking feature northeast of Kodiak Island. This feature temporarily disrupts the flow through the Strait during the Fall.....60-61

Figure 19: Model solution for January 15, 1988 showing the anticyclonic feature near 58° N, 136° W, which is similar to the Sitka eddy. It is found at various times throughout the model solution. The model result conflicts with observations in that the model eddy is smaller than the observed Sitka eddy and the model eddy does not migrate..... 63

the model eddy is smaller than the observed Sitka eddy and the model eddy does not migrate..... 63

Figure 20: The model generates a cyclonic eddy feature shown by the circular purple contours northwest of Queen Charlotte Island. The eddy forms in January and persists until May.

Its formation is believed to be a result of wind forcing and topographic effects in conjunction with potential vorticity conservation 64

Figure 21a-b: The upper(a) and lower(b) figures show the annual variability of the cyclonic eddy feature northwest of Queen Charlotte Island. There is considerable decrease in the size of the feature (based on contours of ULT shown) from February 9, 1987 to February 9, 1988. This figure demonstrates the interannual variability of the model solution 65

Figure 22: Contours of model transport (in Sverdrups) for 1986 through 1988 integrated over one half degree bands along five degree transects south of Cordova (upper) and southeast of Kodiak (lower). Station ten is nearest the coast so values there represent transport integrated from the coast to one half degree offshore. Negative values indicate westward transport. The values at station nine are transport values integrated over the half degree band between stations ten and nine, and so on for stations further offshore. In the upper figure we see the seasonal variability of the ACC near station ten (near shore). Transport maxima occur in Spring, minima in Fall, corresponding to the red coastal sea level signal shown in Figure 18a-d. Further offshore (stations 5-1) the transport becomes fairly steady as we approach the interior of the Alaskan Gyre. Southeast of Kodiak (lower figure) we find peak transports occurring in June/July. The concentric contours near stations 9-7 are indicative of the narrowing and intensification of the Alaska Current in this the formation region of the Alaskan Stream. As before we see weakest transports during the Fall. Further offshore the flow becomes fairly steady and there is even some eastward transport (indicated by the positive values) as the transect crosses the center of the Alaskan Gyre (stations 3-1)..... 67

Figure 23: Monthly mean sea level data obtained from PSMSL and NOS. All of the sea level stations are in phase showing no propagating features along the coast..... 69

Figure 24a-c: Raw power spectra of hourly NOS sea level data. propagating features along the coast..... w

Figure 24a-c: Raw power spectra of hourly NOS sea level data. The majority of the energy lies in the diurnal and semi-diurnal frequency bands (spikes at 0.0805 and 0.041). Additional energy

is contained in the annual signal (spike at 0.2×10^{-3}) and fortnightly tides (spike at 3.1×10^{-3}). Little energy was found at the "storm band" frequencies of four to ten days. The scale of the abscissa is changed to allow the reader to examine details of the spectra. Other stations yielded similar spectra, Sitka chosen for example only70-71

Figure 25a-b: Comparison plots of filtered NOS MSL versus model "h" field data. The southeastern most station, Neah Bay, agrees exceptionally well with the model (a). At Sitka, however, there is poor agreement in amplitude and phase (b)..... 72

Figure 25c: This figure shows improved agreement at Kodiak, but it is still not as good as Neah Bay..... 73

Figure 26a-b: The upper figure shows the free surface deviation for the NOARL Pacific basin model. The NOARL model coastline is plotted as the 200 meter isobath. Visual comparison of the model result for the same month (lower figure) with the NOARL model is excellent. Both ULT and free surface deviation are analogous to sea surface height..... 76

Abstract

A wind-driven, non-linear, reduced gravity, primitive equation model is used to simulate the circulation of the northeast Pacific Ocean. The model includes bottom topography and coastal geometry. The model domain encompasses the entire Gulf of Alaska region from south of Vancouver Island to just west of Kodiak Island. This region is traditionally beyond the bounds of applicability of the reduced gravity model, and this research tests some of the limits of its use. The model resolution, 1/40th of a degree, is exceedingly fine, and we expect that it would allow the mesoscale eddy field to develop. This is the first time that a model of this type and resolution has been successfully run at these latitudes. Twenty years of COADS pseudo wind stress data are analyzed statistically to obtain a wind stress climatology. After spin-up, the monthly stress for 1986-1989 is used to drive the model. The model solution is explained by the dominant spatial patterns seen in the EOF analysis of the forcing wind field. The model reproduces many of the regional oceanographic features such as the Alaskan Gyre, the Alaska Current, the Alaska Coastal Current, the Sitka eddy, and an intense, cyclonic eddy (that has not yet been reported in the literature) northwest of Queen Charlotte Island in the spring. In addition, these model features display seasonal and interannual variability. Model results are validated through comparisons with NOS coastal sea level records and a multi-layer, oceanic basin scale model being run at NOARL.

1. Introduction

The northeast (NE) Pacific Ocean is an extremely interesting region of the world's ocean to study from a physical perspective. The region's irregular coastline, large seasonal fluctuations of wind stress, high freshwater discharge rates, and complex bottom topography make for interesting dynamics. There are several benefits to be derived from the study of this region. For example, a knowledge of the circulation may be essential in predicting the dispersal of pollutants such as crude oil from the massive Exxon Valdez spill in Prince William Sound, Alaska in March 1989 [see *Royer et al.*, 1990]. The physical environmental variables which are believed to have a significant impact on fish survival, growth, and migration in the northeast Pacific are temperature, salinity, currents, and parametric measures of stability, turbulence and turbidity [*Mysak*, 1986]. Biotic factors such as the availability of food, competition and predation affect the migration and abundance of fish and are influenced by the physical factors mentioned above [*Mysak*, 1986]. Therefore, the circulation of the NE Pacific Ocean is important to fisheries' activities since the Gulf of Alaska is a major habitat for many species of commercially harvested fish (e.g. salmon, halibut and herring) [*Cummins and Mysak*, 1988]. Variability of the oceanic conditions may be an important factor in the year-to-year changes in stock recruitment and return migration routes of certain fish species. For example, *Hamilton and Mysak* in both joint and independent studies have presented evidence showing that the migration

routes of sockeye salmon may be significantly affected by the "Sitka" eddy (see *Hamilton, 1985; Mysak, 1986; and Hamilton and Mysak, 1986* for details). The NE Pacific may also be important from a global perspective. Low frequency variability in the NE Pacific may be linked to El Niño-Southern Oscillation (ENSO) events in the tropical Pacific through propagating coastal Kelvin waves and disruptions in the general atmospheric circulation caused by ENSO events [*Emery and Hamilton, 1985, Mysak, 1986, Johnson and O'Brien, 1990b*]. Finally, the U.S. Navy has a vested interest in the tactical exploitation of the oceanic fronts and eddies in this region to enhance its submarine warfare and anti-submarine warfare capabilities.

The main focus of this study is to use a wind-driven, reduced gravity model to simulate the circulation of the NE Pacific Ocean and examine the seasonal and interannual variability of the flow. The NE Pacific region is beyond the traditional bounds of applicability for reduced gravity models, and this research tests some of the limits of their use. Twenty years of Comprehensive Ocean Atmosphere Data Set (COADS) pseudo wind stress data were statistically analyzed to obtain a wind stress climatology. After spin-up, the monthly stress for 1986-1989 is used to drive the model. The model reproduces many of the regional flow features such as the Alaskan Gyre, the Alaska Current, the Sitka eddy, and an intense, cyclonic eddy (that has not yet been reported in the literature) northwest of Queen Charlotte Island. We validate model results using NOS coastal sea level records and other data. The study of the model and this region gives us some insight into the seasonal circulation in the Gulf of Alaska and help us

explain its driving mechanisms.

One question we wanted to answer was whether the fine resolution of the model was sufficient to produce many fine scale eddies in this region. Unfortunately, we find that the model does not produce numerous eddies. We believe that the primary limiting factor is the coarse spatial and temporal scales of the forcing wind field. Increasing the number of layers to allow baroclinic instabilities, including thermodynamics, and perhaps even finer resolution may also be necessary to reproduce a rich eddy field. Efforts are being made to extend current work to include forcing from remote coastal Kelvin waves and including freshwater influx from the land.

This paper is divided into six sections. Section two is an overview of the circulation in the NE Pacific Ocean. In Section three we discuss the physical domain, equations and boundary conditions of the numerical model. Analysis of the regional pseudo stress fields used to drive the model is discussed in Section four. Model results and comparisons with sea level data and the NOARL model are presented in Section five. Finally in Section six we present our conclusions.

2. NE Pacific Circulation Overview

The most prominent features of the Northeast Pacific are the eastward flowing North Pacific Current, also known as the Subarctic Current or West Wind Drift, which splits or bifurcates near the North American coast at approximately 45° N into the southward flowing California Current and the northward flowing Alaska Current [Dodimead *et al.*, 1963]. Figure 1 shows the major features of the general circulation of the region. The Alaska Current forms the eastern branch of the large scale wind-driven cyclonic circulation in the Gulf of Alaska. It eventually converges near Kodiak Island into the intense, westward flowing Alaskan Stream [Tabata, 1982]. Shoreward of the Alaskan Stream lies the Alaska Coastal Current (ACC). In addition, there is a quasi-permanent anticyclonic feature a few hundred kilometers west of Sitka, Alaska called the "Sitka eddy" [Tabata, 1982].

2.1 The Alaskan Stream

The Alaskan Stream is an extension of the Alaska Current which narrows and intensifies near 150° W, and flows westward along the Alaskan Peninsula and Aleutian Islands (see Fig. 1) providing a source of dilute surface water, and relatively warm (4° C) water to depths of 300 meters in the northwestern North Pacific Ocean [Dodimead *et al.*, 1963; Favorite, 1967]. In addition to the work by Dodimead *et al.* and Favorite, there have been numerous studies of the Alaskan Stream conducted over a

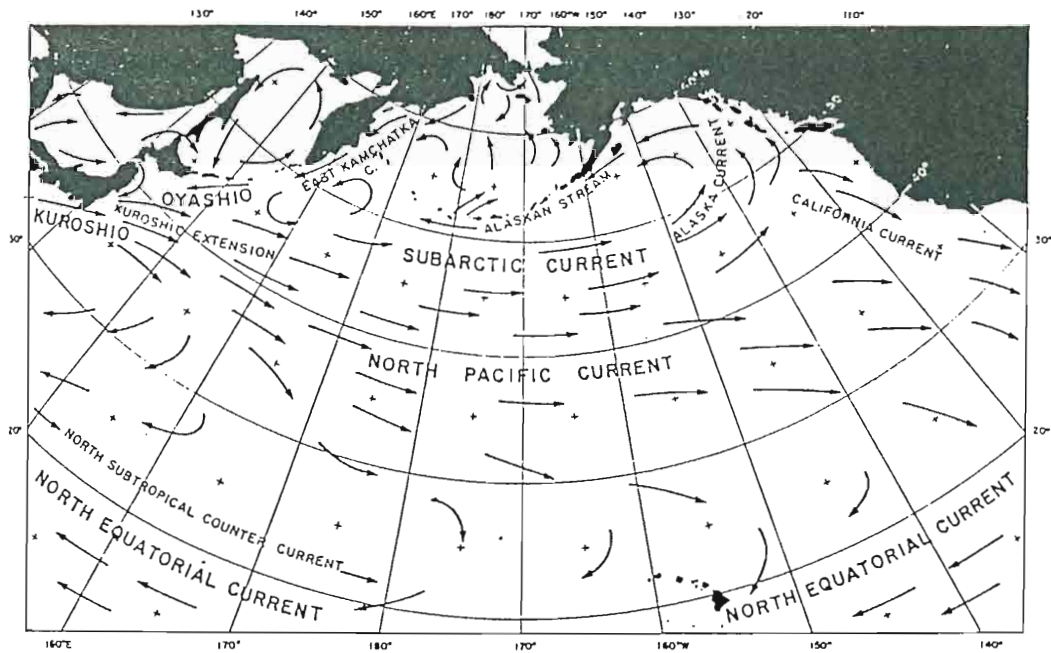


Figure 1: Major surface currents of the North Pacific Ocean (from *Tabata, 1976*). The major currents of the NE Pacific region include the Subarctic Current, the Alaska Current, and the Alaskan Stream.

period of many years including work done by *Reed and Taylor* [1965], *Favorite et al.* [1976], *Reed et al.* [1980], *Reed et al.* [1981], *Reed* [1984], *Reed and Schumacher* [1984], *Royer and Emery* [1987], *Warren and Owens* [1988], and *Reed and Stabeno* [1989]. These studies tend to support earlier works and are in general agreement with each other. There are, however, some disagreement on certain specific points which will be discussed later in this section.

Favorite [1967] concluded that the water driven northward into the Gulf of Alaska by wind stress curl moves westward along the the Alaskan Peninsula and Aleutian Islands as a narrow, intense boundary flow whose characteristics are a result of vorticity conservation [*Reed et al.*, 1981]. *Favorite* [1967] states that the stream is bounded on both sides by lines of zero velocity, and it will contain no potential vorticity (PV), nor will it transport any PV. Therefore, he continues, the total counterclockwise (CCW) vorticity of the stream is reduced in the direction of the flow.

The physical limits of the width of the stream are marked by weak eastward flow seaward of the Alaskan Stream and the inshore edge of the stream is unambiguously defined by a flow reversal (towards the east), or by a zone of weak flow that makes no contribution to the transport [*Reed et al.*, 1980]. These flow reversals and weak flows were also identified by *Royer et al.* [1990] as the seaward limit of the ACC which will be discussed in the next section. The inshore edge of the stream is frequently in water deeper than 300 m [*Reed et al.*, 1980].

...the westward flow in the Alaskan
300 m [*Reed et al.*, 1980].

There is a general continuity of the westward flow in the Alaskan Stream from 160° W to 170° E [*Favorite*, 1967]. Near 170° W the flow splits

(this split may be influenced by the Komandorski Ridge) into a northward branch which flows into the Bering Sea, and a southward branch which eventually rejoins the Subarctic Current [*Favorite*, 1967]. *Dodimead et al.* [1963] used the horizontal distribution of surface salinity and subsurface maximum temperature to infer the path and continuity of the Alaskan Stream [*Reed et al.*, 1980]. As expected, these property distributions are closely paralleled by the geopotential topography [*Reed et al.*, 1980]. Furthermore, sigma-t sections obtained by *Reed* [1984] closely parallel the salinity structure, which accentuates the fact that salinity, not temperature, mainly controls the density in the region.

It appears that the stream is more coherent in the vertical than in the horizontal. Vertical correlation coefficients in the along stream direction were > 0.8 , but were only 0.3-0.4 in the cross stream direction [*Reed and Schumacher*, 1984]. The major characteristic of the flow is that velocity constantly decreases with depth [*Reed and Schumacher*, 1984].

Earlier measurements and computations of the velocity in the Alaskan Stream are supported by more recent studies. *Favorite* [1967] observed velocities near Atka and Adak islands in excess of 100 cm s^{-1} , but maximum geostrophic velocities (referred to 1000 db) were only 30 cm s^{-1} . Maximum observed ship drift speeds were on the order of 80 cm/sec with an average of 50 cm s^{-1} ; U.S. Coast and Geodetic Survey drogues measured maximum velocities $> 100 \text{ cm s}^{-1}$ with an average of 75 cm s^{-1} in the direction of 270° T [*Favorite*, 1967]. *Reed et al.* [1981] found the highest maximum velocities $> 100 \text{ cm s}^{-1}$ in the direction of 270° T [*Favorite*, 1967]. *Reed et al.* [1981] found the highest geostrophic speeds were at the mooring sites where computed surface speeds (referred to 1500 db) exceeded 100 cm s^{-1} , and estimates of ship drift

were also $\sim 100 \text{ cm s}^{-1}$. These measurements took place during February-March 1980. *Reed and Schumacher* [1984] suggest that the Alaskan Stream in this region has a baroclinic structure that is approximately geostrophic. They also found at their deep mooring, station 2 near Kodiak Island, the direction of the net flow was virtually the same at all levels, and speeds decreased with depth as expected.

Initial volume transports computed from the geostrophic currents near Adak Island were approximately $6 \times 10^6 \text{ m}^3 \text{ s}^{-1}$ [*Favorite*, 1967]. Wind-driven transport integrated across 50° N between 155° W and the North American Coast amounted to $5.2 \times 10^6 \text{ m}^3 \text{ s}^{-1}$, essentially balancing the observed transport in the Alaskan Stream [*Favorite*, 1967]. *Reed et al.* [1980] computed transports nearly three times greater than those computed by *Favorite*. They computed a mean volume transport (adjusted to 1500 db) of $12 \times 10^6 \text{ m}^3 \text{ s}^{-1}$ with minimum and maximum values of 8 and $17 \times 10^6 \text{ m}^3 \text{ s}^{-1}$, respectively. Long-term integrated total wind-driven transports in the gulf cited by *Reed et al.*, [1980] obtained from an unpublished report by *Ingraham et al.*, [1976] vary from about $20 \times 10^6 \text{ m}^3 \text{ s}^{-1}$ in winter to less than $5 \times 10^6 \text{ m}^3 \text{ s}^{-1}$ in spring and summer, with considerable year to year variations. The concurrence between the observed transport and the transport calculated from wind stress supports the theory that the Alaskan Stream is driven primarily by the action of the wind over a broad region of the northeast Pacific Ocean [*Favorite*, 1967]. The observed narrowness of the stream and continuity of transport also support the view that it is a western boundary current related to the general distribution of wind stress [*Favorite*, 1967]. The most striking feature about the wind stress transport

is the order-of-magnitude change from winter to spring and summer [Reed *et al.*, 1980]. Large values usually occur as early as October and persist through February or March [Reed *et al.*, 1980]. Integrated model transports (to be discussed in section five) are in general agreement with these findings.

Spatial changes in transport of the stream do occur. They occur in three major ways: (1) loss of water to the south or by recirculating around the Alaska gyre; (2) gain of water from the south (Subarctic Current), usually west of 175° W; and (3) loss of water to the north through some passes in the western Aleutians [Reed *et al.*, 1980]. More recent studies by Reed and Schumacher [1984] imply that the stream moves laterally, in a vertically coherent manner which is supported by Reed and Stabeno [1989].

Although integrated wind-stress curl over the Gulf of Alaska (presumably the driving mechanism for the Alaskan Stream; Favorite, 1967]) increases by an order of magnitude from summer to winter, it is not clear if the stream has any seasonal variation in baroclinic volume transport [Reed, 1984]. The data presented by Reed *et al.* [1980] do not support the existence of any significant seasonal variation in the baroclinic transport that could be associated with the large scale seasonal changes in the wind stress over the Gulf of Alaska. In fact, the correlation coefficient between the mean wind stress transports and observed transports was only 0.04 [Reed *et al.*, 1980]. On the other hand, Royer [1981] indicated that there was a 90% probability of seasonal variation in the Alaska Current (which he uses synonymously with Alaskan Stream) of magnitude $1.2 \times 10^6 \text{ m}^3 \text{ s}^{-1}$. Royer [1981] further states that this variation is 13% of the mean flow which

is higher than that of the Gulf Stream (8.5% of its mean flow). *Reed et al.* [1980] reported that *Ohtani* [1970] and *Favorite et al.* [1976] concluded that baroclinic transports were fairly constant. *Reed et al.* [1980] believes that although rather large changes in transport do occasionally occur, they do not appear to be seasonal in nature. *Reed et al.* [1981] found the weekly net flow at 980 meters over a period of six months to be typified by low frequency variability. More evidence from *Reed and Stabeno* [1989] supports the findings of others that the stream may move laterally offshore; the mechanism for which is not known. Moreover [*Reed and Stabeno*, 1989] feel that the weak flows they saw in their data were anomalous.

It appears that the the baroclinic flow does not consistently spin up or down seasonally because of insufficient response time at these high latitudes [*Reed et al.*, 1980]. *Royer and Emery* [1987] feel that the controversy over the variation in the circulation in response to variation in the wind stress and wind stress curl implies that either the ocean's response to wind forcing is more complex than we think, or our measures of winds and/or currents are inadequate. Seasonal changes appear to be confined to the upper layer and to have little effect on the system as a whole [*Reed*, 1984].

Reed et al. [1981] examined weekly mean deviations in sea level, after adjustment for variations in atmospheric pressure, recorded at the National Ocean Survey tide gauge on Kodiak Island, but were not able to find any obvious correspondence with their own velocity record. They ~~concluded that the velocity fluctuations in deep water over the slope did not seem to have large effects that were transmitted over the shelf and were~~ find any obvious correspondence with their own velocity record. They concluded that the velocity fluctuations in deep water over the slope did not seem to have large effects that were transmitted over the shelf and were

readily apparent at the coast. *Reed et al.* [1981] reported that similar results were found by *Brooks and Bane* [1981] off the coast of North Carolina.

Reed et al. [1981] found the Alaskan Stream to have KE'/\overline{KE} ratios that were roughly an order of magnitude less than those found in the Gulf Stream and Antarctic Circumpolar current. Even though *Reed et al.* [1981] stressed the low-frequency variability of the Alaskan Stream, its fluctuating energy levels in relation to the mean kinetic energy appear to be much lower than those in the Kuroshio, Gulf Stream, and Antarctic Circumpolar Current. Why does the Alaskan Stream appear to be more stable than these other boundary currents? *Reed et al.* [1981] suspect that it results from differences in the direction of these flows in relation to the bottom topography. *Reed and Schumacher* [1984] also concluded that the eddy energy in the Alaskan Stream is generally less than in these other boundary currents in comparable flow regions and the KE'/KE ratios are also typically smaller in the Alaskan Stream than in the Kuroshio or Gulf Stream where the net flows are similar. Hence the Alaskan Stream seems to be a more stable flow than typical western-boundary currents *Reed and Schumacher* [1984]. Whereas western-boundary currents are typified by appreciable variance in the intermediate or mesoscale band of 20-70 days, results from fairly long term current meter measurements in the Alaskan Stream revealed a stable flow with most of the energy at low frequencies (<0.2 cpd) [*Reed and Schumacher*, 1984; *Reed and Stabeno*, 1989]. This contrasts with the Kuroshio and Gulf Stream, which are characterized by (<0.2 cpd) [*Reed and Schumacher*, 1984; *Reed and Stabeno*, 1989]. This contrasts with the Kuroshio and Gulf Stream, which are characterized by intense eddylike features [*Reed and Stabeno*, 1989].

2.2 The Alaska Coastal Current

Shoreward of the inner edge of the Alaskan Stream lies the Alaska Coastal Current (ACC) (see Fig. 2). The presence of the ACC is mainly due to two factors; 1.) high rates of freshwater discharge and 2.) intense wind stresses [Royer *et al.*, 1990]. Royer *et al.* [1990] points out that the average annual amount of freshwater entering the NE Pacific drainage system is at least 20% greater than the the Mississippi River system, and the seasonal signals of wind stress and wind stress curl are the largest in the North Pacific. Because the coastal drainage region is narrow (< 100 km), the majority of the freshwater entering the regime is from small, short streams, rather than from large river networks [Royer *et al.*, 1990]. Thus, the freshwater enters as a distributed or line source, vice a large single source such as the Mississippi River [Royer *et al.*, 1990]. The Gulf of Alaska is infamous for the frequent storms that pass through the region. The Pacific Ocean provides the energy and moisture for these storms to the atmosphere. The cyclonic (counterclockwise) storm systems that provide precipitation for freshwater runoff also supply wind stresses that create coastal convergences and downwelling of surface waters [Royer *et al.*, 1990]. The easterly winds associated with the low pressure storm systems move surface water to the right (in the northern hemisphere), causing an accumulation or convergence of surface water near the coast [Royer *et al.*, 1990]. The coastal downwelling and associated convergence maintains the freshwater as a near shore feature and enhances the density related nature of the flow [Royer *et al.*, 1990].

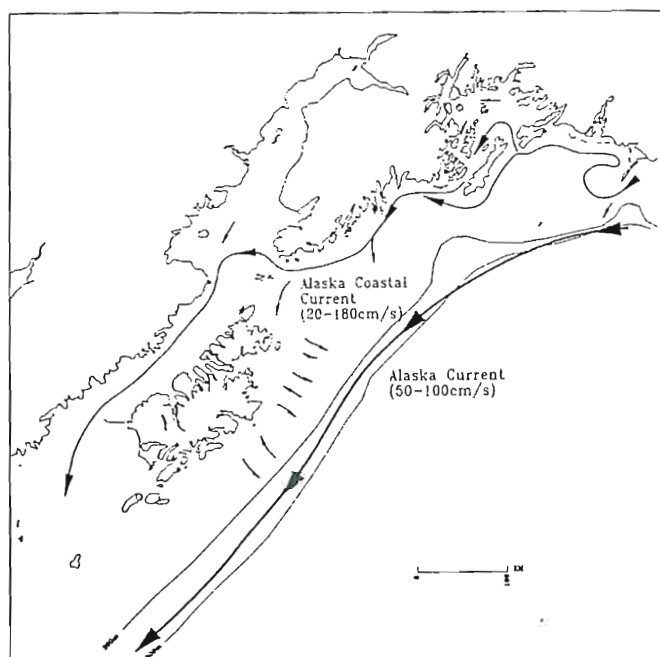


Figure 2: Schematic diagram of the surface circulation for the northwest Gulf of Alaska showing the Alaska Coastal Current in relation to the Alaska Current near Kodiak Island (from Royer *et al.*, 1990). The relatively dilute ACC hugs the shoreline while the Alaska Current remains on the continental slope. Current velocities are similar, but the transport of the ACC is an order of magnitude less than that of the Alaska Current.

Figure 2: Schematic diagram of the surface circulation for the northwest Gulf of Alaska showing the Alaska Coastal Current in relation to the Alaska Current near Kodiak Island (from Royer *et al.*, 1990). The relatively dilute ACC hugs the shoreline while the Alaska Current remains on the continental slope. Current velocities are similar, but the transport of the ACC is an order of magnitude less than that of the Alaska Current.

The relatively dilute ACC has an intense westward velocity (20-180 cm s⁻¹) and is confined mainly to within 20 km of the shore [Royer *et al.*, 1990]. Density driven transports in the upper 100 m are about 2×10^5 m³ s⁻¹ with seasonal fluctuations of about 1×10^5 m³ s⁻¹ [Royer *et al.*, 1990]. Due to the sea surface tilt, the velocity component of the ACC is always westward [Royer *et al.*, 1990]. Modal analysis of currents, winds and freshwater discharge indicates that the primary mode of the alongshore flow component is nearly all due to sea level slopes and is related to the upwelling index, a measure of the onshore-offshore Ekman transport [Royer *et al.*, 1990]. Seaward of the ACC Royer *et al.*, [1990] found transient density-induced flow reversals and small transport values. These are essentially the same as those found by Reed *et al.*, [1980] shoreward of the Alaskan Stream. Due to a lack of freshwater influx and steady wind forcing, and in the presence of island groups and complex bottom topography the ACC spreads laterally across the shelf as it moves southwestward along the Alaskan Peninsula [Royer *et al.*, 1990]. The lateral extent of the ACC is shown in Figure 2.

2.3 The Sitka Eddy

The Sitka eddy is a recurring, well developed, anticyclonic baroclinic eddy whose diameter ranges from 200 to 300 km and whose depth extends to 1000 m, and possibly to as deep as 2000 m [Tabata, 1982]. The Sitka eddy is usually found within a few hundred kilometers of Sitka, Alaska in the vicinity of 57°N, 138°W (Fig. 3) [Tabata, 1982]. The average surface speed of the eddy, at about 50 km from the center, is approximately 15 cm s⁻¹

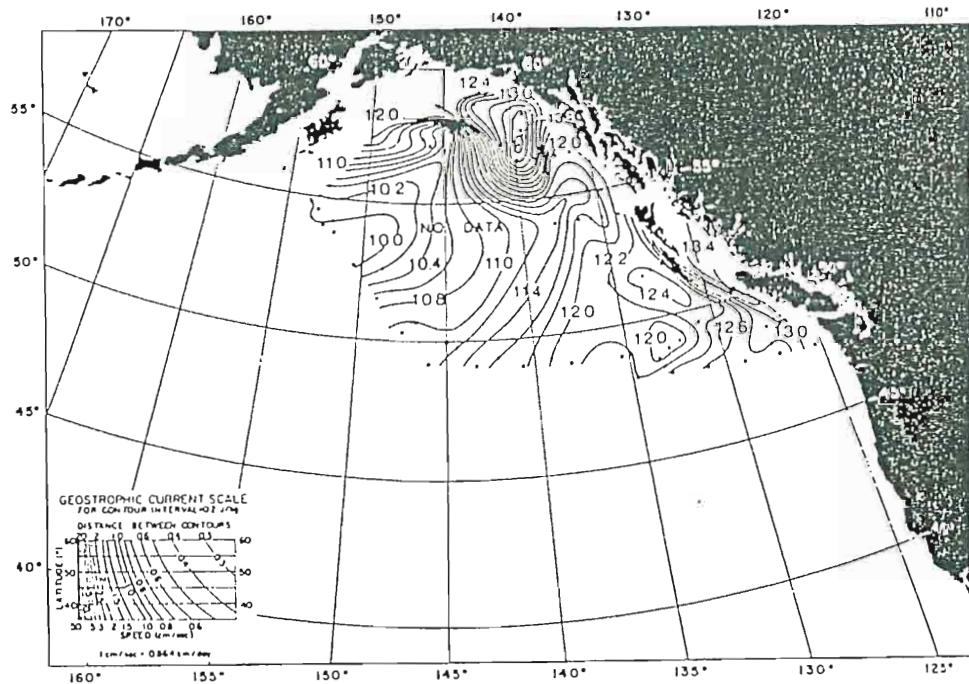


Figure 3: Geopotential anomaly at the sea surface relative to the 1000 db surface in the northeast Pacific during March-April 1958 (from *Tabata*

Figure 3: Geopotential anomaly at the sea surface relative to the 1000 db surface in the northeast Pacific during March-April 1958 (from *Tabata*, 1982). The Sitka eddy is centered at 57° N 140° W. The size of the Sitka eddy is greater than the feature generated by the model. The reader should notice that there is no data southwest of the eddy center.

(relative to 1000 db), with a maximum value reaching almost 40 cm s^{-1} [Tabata, 1982]. The average baroclinic transport in the upper 1000 db layer is $5 \times 10^6 \text{ m}^3 \text{ s}^{-1}$, with a maximum approaching $8 \times 10^6 \text{ m}^3 \text{ s}^{-1}$ [Tabata, 1982]. The transport of the eddy is mainly confined to the upper 500 meters [Tabata, 1982]. Drifting buoy data, on the other hand, show the average speed of the eddy to be about 70 cm s^{-1} (at about 70 km from the center), with a possible maximum daily speed of 110 cm s^{-1} [Tabata, 1982]. The eddy appears to propagate westward at a minimum rate of 1.5 km d^{-1} , which is consistent with the Rossby wave propagation speed of $\sim 1 \text{ km d}^{-1}$ [Tabata, 1982].

The eddy appears to have formed locally (there is little evidence to show that it drifts into the area from elsewhere), and to have persisted for up to at least a year and a half as it propagates westward [Tabata, 1982]. The three most important eddy generating mechanisms for this eddy appear to be atmospheric forcing, topographical interaction, and baroclinic instability of the mean currents [Tabata, 1982]. Attempts to relate the eddy to the distribution of the wind stress curl and to the variability of the observed mean sea level along the nearby coast did not yield conclusive results [Tabata, 1982]. While local atmospheric forcing may not be the generating mechanism for the eddy, it may be the source of energy needed to sustain the eddy [Tabata, 1982]. Willmott and Mysak [1980] suggested that the generating mechanism for this and other Northeast Pacific eddies is atmospherically-forced baroclinic Rossby waves that undergo multiple reflections along the coasts of British Columbia and Alaska [Mysak, 1985]. It is atmospherically-forced baroclinic Rossby waves that undergo multiple reflections along the coasts of British Columbia and Alaska [Mysak, 1985]. It was recognized, however, that topographical interactions could

contribute to the production of the Sitka eddy, and local topography may be why the eddy seems to form near the same location year after year [Tabata, 1982; Mysak, 1985]. Swaters and Mysak [1985] have proposed a theory for the generation of the Sitka eddy by the interaction of a steady coastal current with a variable bottom topography [Mysak, 1985]. It may be difficult to separate the two proposed generating mechanisms for the Sitka eddy (topographic interaction: Swaters and Mysak, 1985; and superposition of forced Rossby waves: Willmott and Mysak, 1980). However, on the short time scale, the initial formation of the eddy could be due to mean flow-topographic interaction, but once the eddy is formed, long time scale dynamics associated with interannual baroclinic Rossby waves becomes important and produces the westward drift of the eddy which has been observed by Tabata [1982] [Mysak, 1985].

The eddy is not readily apparent from the distribution of temperature in the surface layer, but it is most distinguishable in the water properties below 100 m [Tabata, 1982]. The center of the eddy is featured by the presence of a warm core within the halocline which usually occurs at depths from 100 to 200 m (occasionally to 300 m) [Tabata, 1982]. The halocline at the center is usually depressed [Tabata, 1982]. Finally, the water at the center from 100 to at least 1000 m is warmer, less saline, and contains more dissolved oxygen than at corresponding depths away from the center [Tabata, 1982].

2.4 General Bathymetry of the Region

Tabata [1982] observed that the bathymetry of the northeast corner of

the Pacific Ocean (see Fig. 4) is characterized by a relatively large area of abyssal plain whose depth ranges from 3000 to 5000 meters. Within this area he noted that there are a number of seamount ranges and guyots which rise abruptly from the ocean floor. In particular, he points out that there is a chain of features that stretches northwestward from the Queen Charlotte Islands to near Kodiak Island. In general, their depths range from 500 to 1000 meters, but some are as shallow as 44 meters. To the south and parallel to the Aleutian Islands lies a fairly deep trench with depths exceed 5000 meters. This trench is situated approximately 150 km south of Kodiak Island. The width of the continental shelf (distance from shore to the 200 meter isobath) in this region varies from a minimum of less than 25 km off the west coast of Queen Charlotte Islands, to 30 km off Baronof and Chigagof Islands, to 90 km off Yakutat, to a maximum of 160 km east of Kodiak Island [Tabata, 1982]. The continental slope is relatively steep; its depth generally increasing seaward from 200 to 2000 meters within 25 km [Tabata, 1982]. Although the slope is oriented parallel to the coast, irregular features become noticeable beyond the 2000 meter contour, with ridges and depressions occurring at a number of locations [Tabata, 1982].

2.5 Climatology

The wintertime climatological wind pattern of the Gulf of Alaska is dominated by the presence of the Aleutian low which stretches from Kamchatka to the Alaskan Peninsula with a weak high pressure off the southern California coast [Emery and Hamilton, 1985]. Summertime circulation is weaker than the winter pattern; the Aleutian low remains,

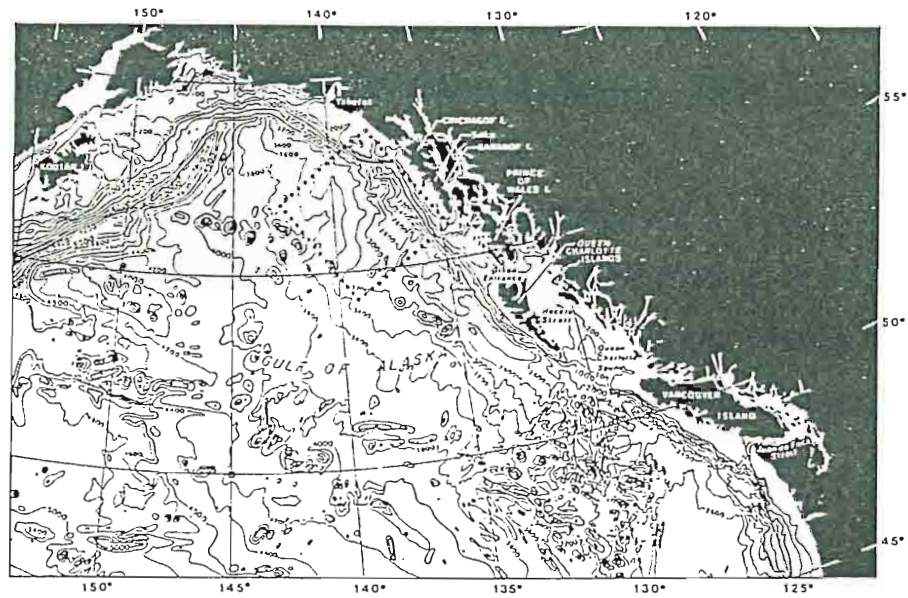


Figure 4: Bottom topography chart for the NE Pacific Ocean region. The general area of the Sitka eddy is indicated by the dotted square (from *Tabata* [1982]).

but is weaker and is shifted to the northwest while the California high has strengthened and expanded into the southeastern part of the Gulf of Alaska [Emery and Hamilton, 1985]. The winter pattern has three basic patterns, (1) similar to the mean, (2) more intense than the mean, and (3) weaker than the mean [Emery and Hamilton, 1985]. Changes in these patterns have been related to El-Niño/Southern Oscillation (ENSO) events (see Emery and Hamilton, 1985 for details).

Analysis of COADS pseudo stress, outlined in section 4, shows that the wind stress in the NE Pacific is strongest during the winter months (Dec-Feb) and weakest during the summer months (Jun-Aug). Spectral analysis shows that the highest energy is contained in the annual signal.

3. The Model

3.1 Background

The FSU Northeast Pacific Model is a nonlinear, reduced gravity, primitive equation model with one dynamically active layer above an inactive deep layer. This model simulates the first baroclinic mode from which we expect to be able to estimate interannual variabilities of surface currents, thermocline depth, and sea level along the northeast Pacific Coast. The interface between the two layers simulates the ocean pycnocline. Figure 5 is a cross sectional view of a typical one and one-half layer model.

The model domain (see Figure 6) extends from 45° to 60° N and from the West Coast of North America to 155° W. The domain encompasses the entire Gulf of Alaska region from south of Vancouver Island to just west of Kodiak Island.

3.2 Equations

The model momentum and continuity equations, in spherical coordinates, are similar to those found in *Johnson and O'Brien* [1990b]. We use the equations in the transport mode for ease in numerical calculations. The model equations are as follows:

use the equations in the transport mode for ease in numerical calculations.

The model equations are as follows:

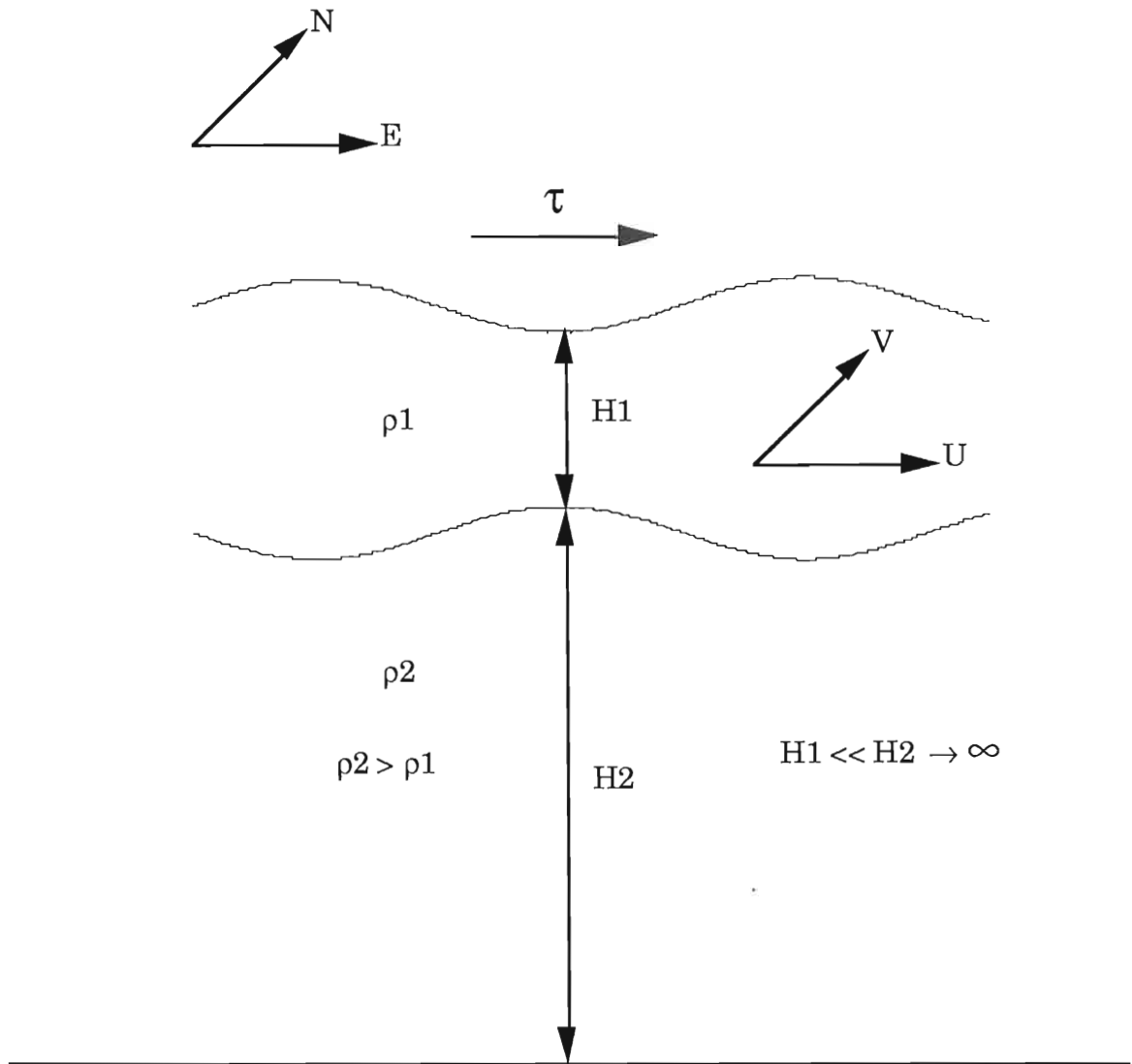


Figure 5: Typical geometry for a reduced gravity model. Only the top layer is dynamically active.

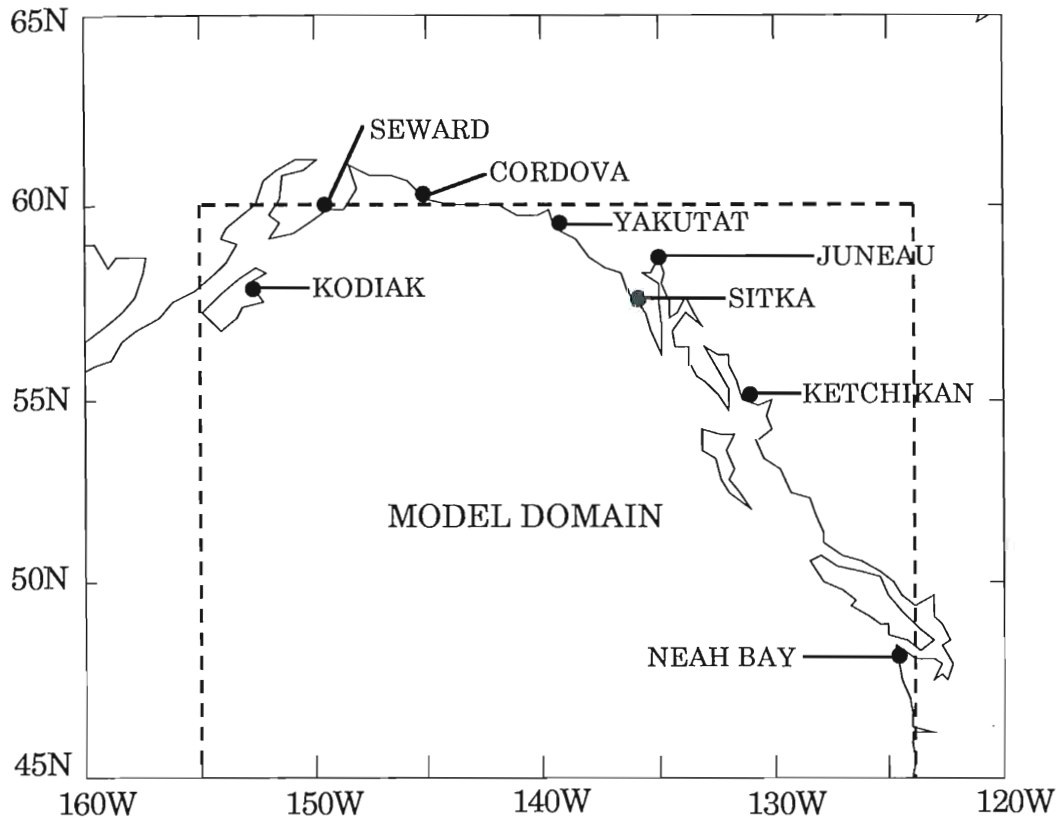


Figure 6: This figure shows the NE Pacific Ocean model region with the

Figure 6: This figure shows the NE Pacific Ocean model region with the model domain outlined by the dashed line. Sea level from selected stations (Neah Bay, Sitka, and Kodiak) is used for model validation. The coastal outline is from the NCAR graphics data base.

$$\begin{aligned} \frac{\partial U}{\partial t} + \frac{1}{a \cos \theta} \frac{\partial}{\partial \phi} \left(\frac{U^2}{H} \right) + \frac{1}{a} \frac{\partial}{\partial \theta} \left(\frac{UV}{H} \right) - (2\Omega \sin \theta)V \\ = - \frac{g'B}{2a \cos \theta} \frac{\partial H^2}{\partial \phi} + \frac{\tau^\phi}{\rho} + AV^2U \end{aligned} \quad (3.1)$$

$$\begin{aligned} \frac{\partial V}{\partial t} + \frac{1}{a \cos \theta} \frac{\partial}{\partial \phi} \left(\frac{UV}{H} \right) + \frac{1}{a} \frac{\partial}{\partial \theta} \left(\frac{V^2}{H} \right) + (2\Omega \sin \theta)U \\ = - \frac{g'B}{2a} \frac{\partial H^2}{\partial \theta} + \frac{\tau^\theta}{\rho} + AV^2V \end{aligned} \quad (3.2)$$

$$\frac{\partial H}{\partial t} + \frac{1}{a \cos \theta} \left(\frac{\partial U}{\partial \phi} + \frac{\partial}{\partial \theta} (V \cos \theta) \right) = 0 \quad (3.3)$$

where ϕ and θ are longitude and latitude, respectively; U and V are transport in the east-west and north-south directions, respectively; H is upper layer depth; $g'=(\Delta\rho/\rho)g$ is reduced gravity; τ^θ and τ^ϕ are the wind stresses applied to the upper layer as a body force; A is the eddy viscosity coefficient; a is the radius of the earth; and Ω is the angular velocity of the earth (values for each of these parameters are given in Table 1). Latitude and longitude increase in the northward and eastward directions, respectively. B is a variable coefficient that adjusts the gravity wave phase speed in relation to bottom topography. Since transport is velocity multiplied by the layer depth, the velocities (u and v) are easily calculated by dividing the layer transports (U and V) by the layer depth (H). See *Dube et al.* [1986] for detailed derivations of the model equations.

Similar models have been used previously to describe the wind driven *al.* [1986] for detailed derivations of the model equations.

Similar models have been used previously to describe the wind driven circulation in the Indian Ocean [*Luther and O'Brien*, 1985], the equatorial Pacific Ocean [*Kubota and O'Brien*, 1988], and the central Pacific Ocean

Table 1. Values of Parameters Used in the Model

<u>Parameter</u>	<u>Symbol</u>	<u>Value</u>
Reduced gravity	g'	0.0067 m s^{-2}
Radius of the earth	a	$6.37 \times 10^6 \text{ m}$
Density of seawater	ρ	1025 kg m^{-3}
Earth's angular velocity	Ω	$7.292 \times 10^{-5} \text{ rad s}^{-1}$
Eddy Viscosity Coefficient	A	$150 \text{ m}^2 \text{ s}^{-1}$
Drag Coefficient	C_D	1.5×10^{-3}

[Pares-Sierra and O'Brien, 1989]. Note that this model provides no information about the vertical structure of the ocean, except for an estimate of the thermocline depth, nor does it contain any thermodynamics.

In order to resolve features such as fronts and eddies, the minimum Δx , Δy must be less than the Rossby radius of deformation (R_0) which is approximately equal to 3-11 km for the latitude range of the NE Pacific. Model resolution is 1/40th of a degree in both the zonal and meridional directions, resulting in a grid spacing of 1.4 km (at 60° N) which is less than the deformation radius. This is the first time a model of this high resolution has been run at these latitudes for large scale upper ocean wind driven variability.

The time step is five minutes (one model year takes 4.2 hours to run on one processor of the Cray YMP). The model array size is 621 x 301 on a staggered "C" grid (see Figure 7) [see Arakawa, 1966 for "C" grid details]. The model utilizes a leapfrog scheme for time integration. Every 21st step, a forward time differencing is used to eliminate the computational mode. The viscous terms are treated using the DuFort-Frankel scheme. The DuFort-Frankel scheme eliminates the need for additional storage in our numerical calculations, and the instabilities that can be produced by this method do not occur in this model due to the small time step used. Details of the numerical scheme can be found in Dube *et al.* [1986].

The model is spun up from a state of rest using climatological wind stress data. The winds are ramped up over a period of 20 days (vice simply turning them on instantaneously) which helps suppress numerical noise and instabilities in the initialization. The wind acts as a body force on the

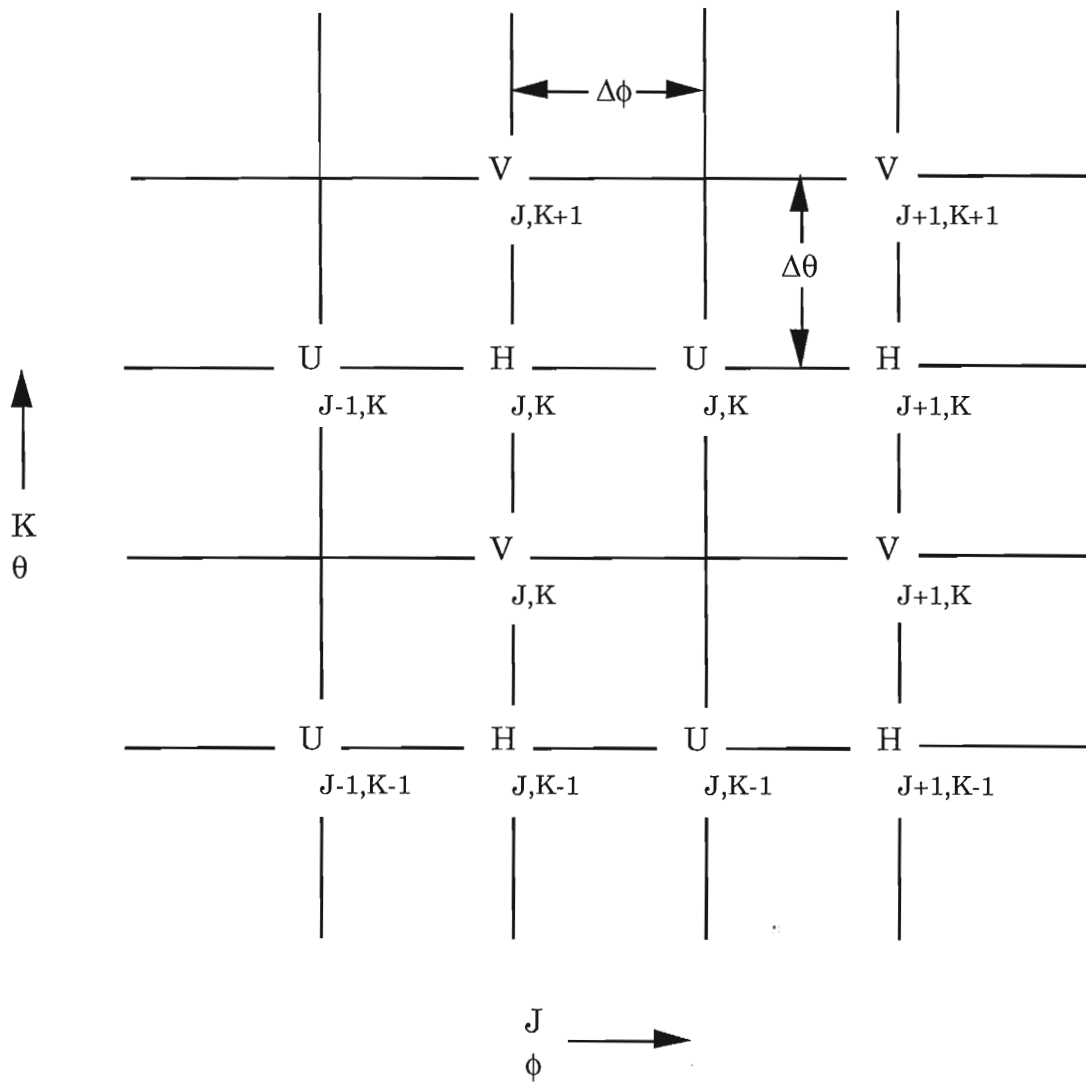


Figure 7: Staggered Arakawa C-grid used in the finite difference discretization of the governing equations, showing the relative locations of U, V, and H.

fluid and is the only forcing imposed on the model except for boundary constraints. The winds used to drive the model were obtained from the Comprehensive Ocean Atmosphere Data Set (COADS) monthly mean pseudo wind stress fields. These wind fields were interpolated to fit the model grid in space and time. Details of the wind stress data analysis and interpolation techniques are discussed in the next section.

3.3 Boundary Conditions

The no-slip boundary conditions ($u=v=0$) are imposed on all coastal boundaries. Open boundary conditions using a variation of the Sommerfeld radiation condition (Eqn. 3.4), are imposed on the southern and western boundaries. On the southern boundary only, the Sommerfeld radiation condition follows that of *Røed and Smedstad* [1984] where the solution is separated into a global (free) and local (forced) solution. The Sommerfeld condition is applied to the local solution, the solution is updated, and added to the global to recover the total solution.

$$\frac{\partial \psi}{\partial t} + F \frac{\partial \psi}{\partial x} = 0; \quad (3.4)$$

where " ψ " is any variable and "F" is determined locally. "F" is the phase speed of the selected variable. When "F" indicates outward propagation (outward from the model domain), values interior to the boundary are projected onto the boundary at the new time. If "F" indicates inward (outward from the model domain), values interior to the boundary are projected onto the boundary at the new time. If "F" indicates inward propagation, the boundary values remain unchanged. This condition allows information to propagate out of the domain while preventing

undesirable information from coming in through the boundary [Camerlengo and O'Brien, 1980]. This condition works well for nondispersive Kelvin waves. It is less successful for dispersive Rossby waves. Therefore, the details of the solution near the western and southern boundaries should be taken with caution.

3.4 Bottom Topography

Effects of bottom topography are incorporated into the model using the methods of *Cushman-Roisin and O'Brien* [1983]. The adjustment is made by a variable coefficient, B , related to the depth of the ocean at a given point. The coefficient at each grid point is determined by the ratio of the upper layer depth divided by the total ocean depth ($B = \frac{H_1}{H_1+H_2(\phi,\theta)}$). This ratio asymptotically approaches one as the depth increases, and has a set minimum value of 0.2 for depths less than or equal to 100 m. This coefficient adjusts the flat bottom phase speed, slowing it along the shallow coast and providing no change in the model interior. As an example, when depths are as shallow as 500-1000 meters, the phase speed can be reduced by as much as 70% of the original value [*Johnson and O'Brien*, 1990a].

If the minimum depth gets too small, i.e. when the model shallows, division by a near zero number causes numerical overflow. Thus, the model upper layer depth is constrained to a minimum value of 100 m. For depths less than 100 m we allow for entrainment from the lower layer. The entrainment technique used follows that of *McCreary et al.*, [1987]. depths less than 100 m we allow for entrainment from the lower layer. The entrainment technique used follows that of *McCreary et al.*, [1987]. However, in the results presented here, this constraint has not been necessary to maintain a stable solution.

We used an initial $H_0 = 300$ meters; resulting in an average phase speed of 1.4 m/sec. This phase speed value is supported by observations, and our choice of parameter definitions for H_0 and g' are supported by other modelling work in this region [see *Cummins and Mysak, 1988*].

An overlay of coastal geographical boundaries on top of model geometry and bathymetry is shown in Figure 8. Both the model geometry and bathymetry were obtained from the National Geophysical Data Center (NGDC) data set.

NORTH PACIFIC MODEL TOPOGRAPHY

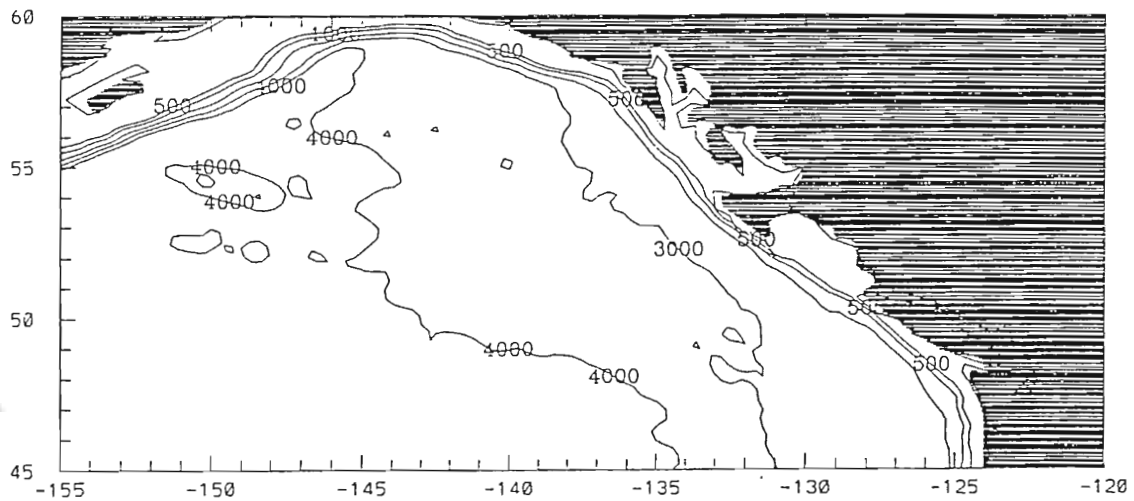


Figure 8: Coastal geometry superimposed on model land boundaries (shaded region) with labelled bathymetry contours. Model land boundaries were defined by the 10 meter isobath with some local adjustments so that the local boundaries look reasonable. It is important to point out that the shallow bank east of Queen Charlotte Island is treated as a solid boundary by the model.

4. Forcing

4.1 COADS Winds

Twenty years (from 1970 to 1989, inclusive) of monthly mean pseudo wind stress was extracted from the Comprehensive Ocean Atmosphere Data Set (COADS) for use in forcing the model. COADS provides average monthly values for several parameters on a $2^\circ \times 2^\circ$ global grid, and we extracted values from 40° - 58° N, 122° - 160° W. A climatological monthly mean pseudo stress from this 20 year data set is used for model spin-up. After spin-up, the monthly mean stress for 1986-1989 is used to drive the model.

Prior to using the wind data to drive the model we examined the data statistically and established a criteria for removing outliers. Data are deleted when there are fewer than five observations for any given month, and, if either the u or v component of the monthly mean pseudo stress is greater than three standard deviations from the 20 year mean. Less than 0.7% of the original data is deleted following this procedure. Missing data values are replaced by interpolated values. The interpolation scheme uses a spatial nine point weighted mesh on the data grid for any given month. Following interpolation, one application of a Hanning Filter (using a 1/4, 1/2, 1/4 weighting) in both the x and y directions is used to eliminate $2\Delta x$ and $2\Delta y$ noise. Figure 9 shows a 20 year time series from the filled and smoothed monthly mean pseudo stress for a COADS grid point central to

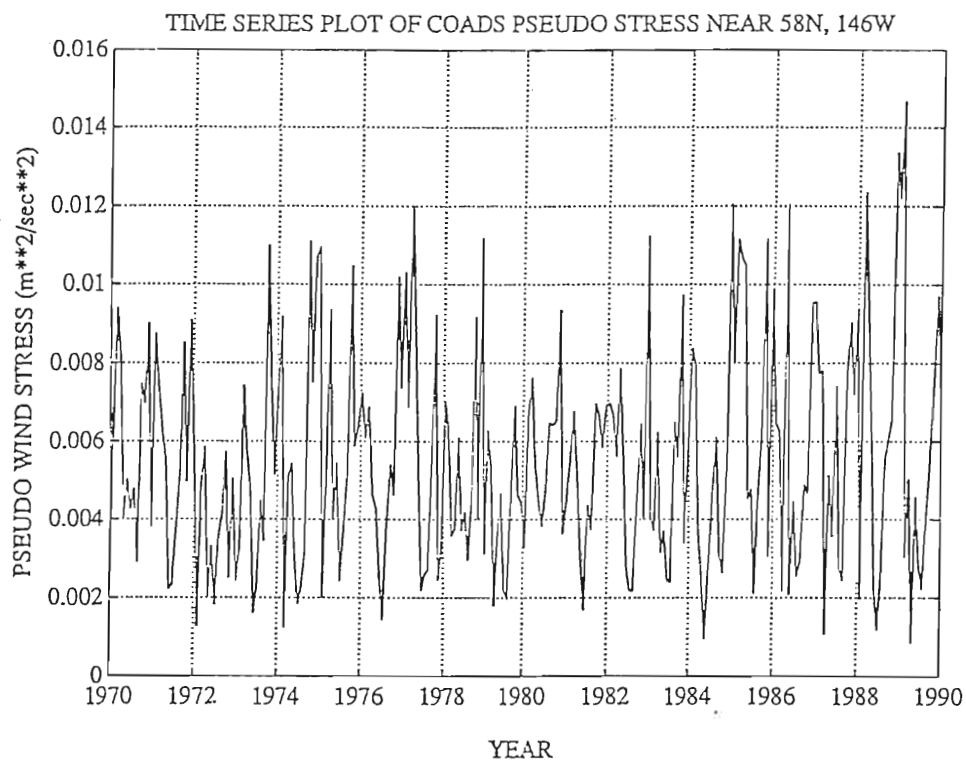


Figure 9: Twenty year time series plot of COADS pseudo wind stress near 58°N , 146°W . Maxima (minima) normally occurring during winter (summer) months. Note the largest maximum occurs in February 1989, and that the maxima trend is increasing.

the model domain. This time series shows that the maximum pseudo stress occurred during winter 1989. In fact, the 20 year time series reveals an increasing trend in the maximum pseudo stress. Typical seasonal wind stress vectors are shown in Figure 10a-c. The magnitude of the stress is generally greatest during the winter months (December-February) and weakest during the summer months (June-August). The power spectrum for the time series is presented in Figure 11. The dominant annual signal strongly influences the model results, as will be shown later.

Because the COADS data are on a $2^\circ \times 2^\circ$ grid, it is necessary to interpolate the pseudo stress to the model grid. This is accomplished using the bi-cubic spline interpolation subroutines found in the International Mathematical Subroutine Library (IMSL). Interpolation in time is also necessary. Monthly mean winds from 1986 to 1989 are linearly interpolated to obtain a new wind value every five minutes as required by the model time step.

We realize the limitations of the COADS monthly winds, and feel it may be worthwhile to obtain finer resolution (in both space and time) wind stress data to drive the model. In addition to the model enhancements to resolve small scale eddies mentioned in section one, high resolution wind stress data may also help generate these features. This is proposed in future work, but is beyond the scope of the present study.

Prior to using the COADS wind stress to drive the model, we computed the curl of the wind stress from the filled and smoothed data. The curl is then analyzed using Empirical Orthogonal Function (EOF) Analysis (also known as Principal Components Analysis). EOF analysis,

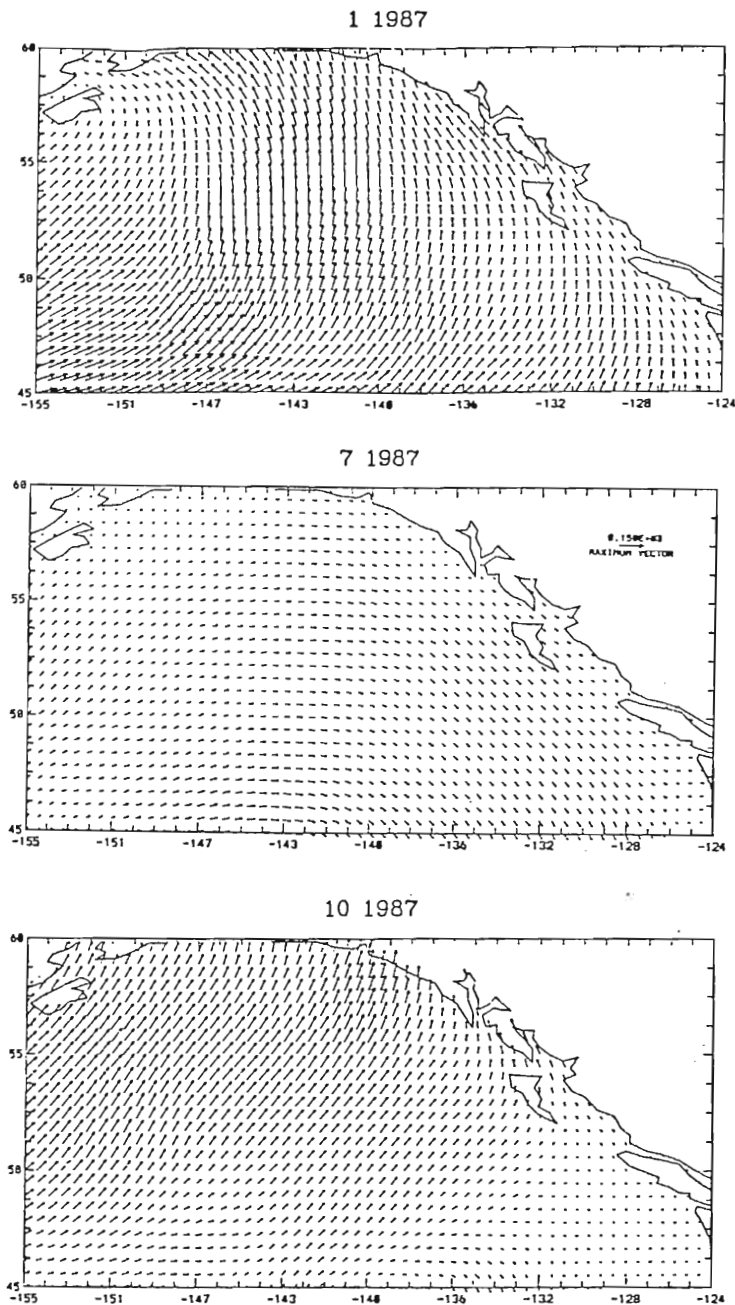


Figure 10a-c: Sample wind stress vectors for (a) January '87, (b) July '87, (c) October '87. Note that the magnitude and direction of the wind stress changes dramatically from summer to winter. During January, the winds in the central basin are northward, turning eastward and weakening considerably by July. By October, the winds strengthen again and begin veering back to the north. Note particularly during October the divergence of the winds near 46° N, 136° W where the current also separates to form the Alaska and California Currents.

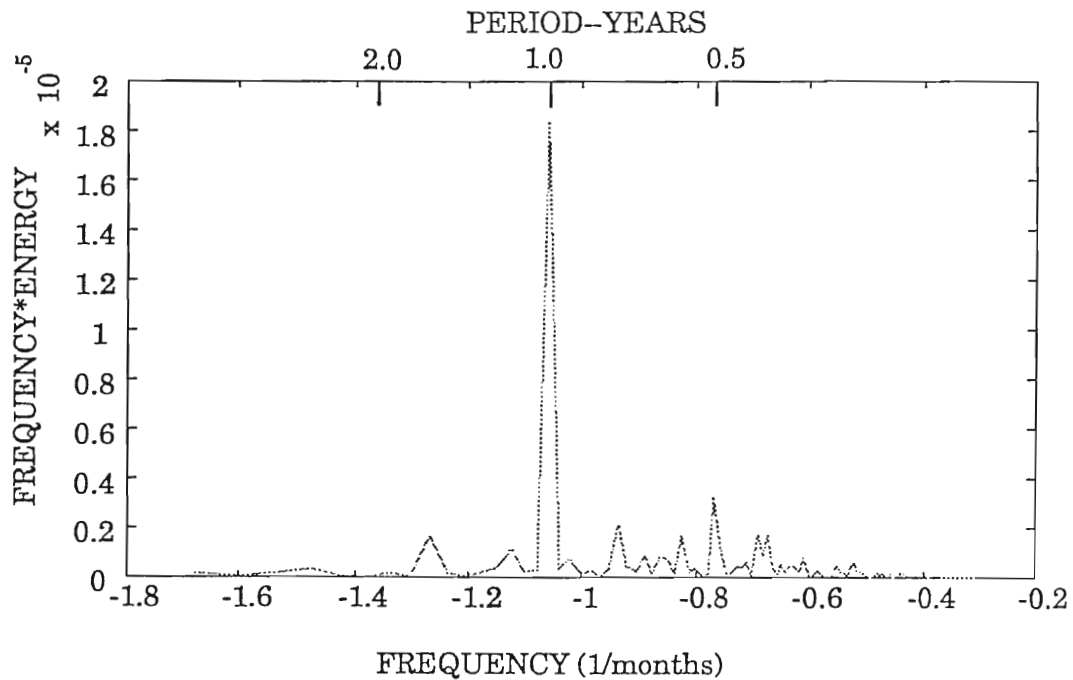


Figure 11: Power spectrum (in variance preserving plot) for the time series shown in Figure 9. The data were smoothed in time with one Hanning

Figure 11: Power spectrum (in variance preserving plot) for the time series shown in Figure 9. The data were smoothed in time with one Hanning pass prior to spectral computation. The winds are clearly dominated by the annual period, with no significant energy present at the "storm band" frequencies (4-10 days). There is additional energy at six and 24 months, evidence of semi-annual and interannual variability of the data.

discussed in detail later in this section, enabled us to examine the seasonal and interannual variability of the pseudo stress, and to examine the link between the spatial and temporal patterns of the data.

4.2 EOF Method

Hardy and Walton [1978] provide an excellent general description of EOF analysis. The analysis begins with an array of observations or measurements arranged into a rectangular matrix. For an appropriate set of measurements taken in time and space, the EOF analysis empirically derives the primary spatial and temporal variations of the data [*Hardy and Walton, 1978*]. The analysis can be performed on vector as well as scalar data which do not have to be equally spaced. EOFs will work independent of the order of the data. The data order becomes significant when the EOF results are mapped back into the spatial or temporal grid.

A correlation matrix or a variance-covariance matrix is formed from the original rectangular data matrix [*Hardy and Walton, 1978*]. The eigenvalues and eigenvectors of the correlation or variance-covariance matrix are then computed. The eigenvectors form a complete orthonormal set of basis vectors which represent the original observations [*Hardy and Walton, 1978*]. When the EOF analysis is completed, the entire data set can be reproduced exactly from the eigenvalues and eigenvectors. The analysis is completely empirical. The following is a summary of the most important properties of EOF analysis (taken from *Hardy and Walton, 1978*):

is completely empirical. The following is a summary of the most important properties of EOF analysis (taken from *Hardy and Walton, 1978*):

1. The relative magnitudes of the eigenvalues can be used to rank order the eigenvectors in terms of decreasing significance in representing the data.
2. The most significant eigenvectors can be identified with physically important patterns in the original data.
3. Temporal expansions of the data in terms of the most significant eigenvectors are known as the principal components.
4. The primary eigenvectors provide a highly efficient basis set for approximating the the original observed data.
5. The eigenvectors and the principal components are derived by an objective mathematical procedure.

The array of pseudo wind stress curl used in the EOF analysis is 171 (space) by 240 (time (months)). The time mean is subtracted from the curl at each point (see Fig. 12) prior to the analysis. This 171 "N" X 240 "M" array (called "W") is then processed by a series of FORTRAN programs designed to compute eigenvalues, eigenvectors, and their associated coefficients. An outline of the process (similar to that of *Legler* [1983], except that the curl is a scalar) follows:

Given some N X M array "W", the eigenvalues " λ_m " exist such that one can find the eigenvectors " E_m " and be able to reproduce the original data matrix exactly (i.e. $W_m = \sum \lambda_m E_m$).

To compute the eigenvalues and eigenvectors, we form the variance-covariance matrix exactly (i.e. $W_m = \sum \lambda_m E_m$).

To compute the eigenvalues and eigenvectors, we form the variance-covariance matrix (call it "C") by multiplying the original data matrix by its

complex conjugate transpose. For computational reasons only it is desirable to form the smallest variance-covariance matrix possible. However, because there was no appreciable gain in computational speed, we elected to form the larger 240 x 240 temporal matrix,

$$[C] = \frac{1}{M} [W][W^{*T}];$$

where W^{*T} is the conjugate transpose of W . C is the sample covariance matrix. The diagonal elements of C are the sample variance, and the off diagonal elements are the covariances. The sum of the diagonal elements of C (commonly known as $\text{TRACE}[C]$) is the total variance in the data

$$\text{TRACE}[C] = \sum_{i=1}^M \lambda_i; \text{ where } \lambda_i = \text{eigenvalues.}$$

The percentage of the total variance accounted for by any of the eigenvalues is easily calculated by $\frac{\lambda_i}{\sum \lambda_i}$. Clearly the largest eigenvalues account for the largest percent of the variance. Each of the eigenvalues has an associated eigenvector, and we find all of the eigenvectors $[E]$ by the eigenvector decomposition of C which is

$$[C][E] = [E][\lambda].$$

$$[C][E] = [E][\lambda].$$

This yields M orthonormal time eigenvectors for each month. From the vectors we extract spatial and temporal coefficients which, when properly

mapped, yield time series and spatial patterns for a given eigenvector. We are primarily interested in the largest eigenvalues and their associated eigenvectors because they account for the largest percent of the variance.

Table 2 lists the percentage and cumulative percentage of the variance for the first nine eigenvectors. The cumulative percentage of all eigenvectors (modes) is 100%. Using the *Overland and Preisendorfer* [1982] significance test for principal components, we determine that the first nine modes are significant at the 95% level. Statistical significance implies that the spatial patterns cannot be reproduced by a spatially and temporally uncorrelated random process (i.e. the spatial patterns are not noise).

4.3 EOF Analysis

The temporal mean subtracted from the data is shown in Figure 12. The physical interpretation of the mean pattern is as follows: The positive curl (cyclonic) in the northwest corner is due to the Aleutian Low, while the negative curl (anticyclonic) in the southern portion is due to the influence of the high pressure cell that dominates the subtropical Pacific.

Our physical interpretation of the mean is supported by climatology. The general atmospheric circulation of the N.E. Pacific can be characterized by the Aleutian Low typically centered at 50°N , 180°W during the winter months. In the spring this low pressure system relaxes and moves northwestward. During the summer months the area is dominated by the Subtropical High usually centered at 35°N , 150°W .

by the Subtropical High usually centered at 35°N , 150°W .

The spatial modes obtained from the EOF analysis are deviations from the mean shown in Figure 12. EOF analysis separates data into

Table 2. Percent and cumulative percent variance for the first nine eigenvectors computed from the curl of the COADS pseudo wind stress data from 1970 through 1989. Over 40% of the total variance is accounted for by the first three modes. The higher modes are attributed to noise.

<u>Mode Number</u>	<u>Percent Variance</u>	<u>Cumulative Percentage</u>
1	21.93	21.9
2	11.77	33.7
3	8.25	42.0
4	5.78	47.7
5	4.76	52.5
6	3.74	56.2
7	3.42	59.7
8	3.26	62.9
9	3.00	65.9

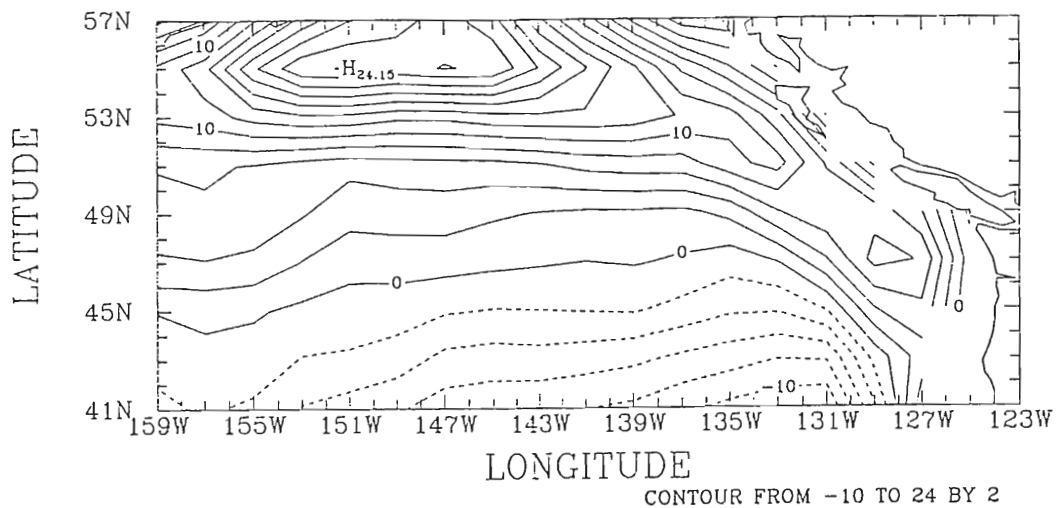


Figure 12: Twenty year temporal mean COADS wind stress curl pattern. Positive values are marked by solid lines, negative values by dashed lines.

Figure 12: Twenty year temporal mean COADS wind stress curl pattern. Positive values are marked by solid lines, negative values by dashed lines. Maxima are marked with an "H", minima with an "L". The large positive (cyclonic) curl in the northwest corner is probably the mean position of the Aleutian Low. The negative contours (anticyclonic) in the southern portion of the figure are evidence of the subtropical high.

major empirical patterns. Signals from one or more physical processes may overlap to produce an EOF mode, making it difficult to relate a single process to a particular EOF pattern.

Interpretation of EOF spatial patterns is based on the known physics of the analyzed data and requires one to examine the spatial picture, the time series and the mean simultaneously. The sign of the time series tells us whether the spatial pattern is strengthened or weakened and whether it adds to or subtracts from the mean. Because we are computing standing EOFs, these modes are interpreted as standing wave patterns.

The most dominant spatial pattern is shown in Figure 13a. This pattern is modulated by the time series shown in Fig. 13b-c. Notice that the positive peaks occur mainly during the winter months. Regions of positive curl are increased when the time series shows large positive peaks and decreased when they are negative. The opposite is true for regions of negative curl. When the time series is near unity, the pattern is as seen in Figure 13a.

One can think of the EOF spatial modes in a manner similar to the vibrating modes of a drum head; therefore, this pattern should be viewed as high and low contours oscillating from positive to negative as modulated by a time series. In the winter of 1978, for example, there is a large positive peak in the time series (see Fig. 13b). The positive region of curl in the southwest of the mode one spatial pattern is increased and added to the mean spatial pattern. This is the annual southward (northward) migration and intensification (weakening) of the Aleutian low in winter (summer). The "H" contour near 55° N, 136° W is probably due to a low

pressure system frequently located in that vicinity. The "H" contour in conjunction with the diagonal band of negative contours establishes a pressure gradient along the coast. This pressure gradient forces an annual coastal sea level signal seen in the model solution which is discussed in detail in the next section.

The power spectrum, for the first mode time series is shown in Figure 13d. All spectra in this section are plotted in variance preserving form and are smoothed in time with one Hanning pass. The majority of the energy for this mode is contained in the annual period. There is also some high frequency energy at eight and six month periods as well as some interannual energy at 18 months.

Eigenvector 2 accounts for 11.77% of the variance, and its spatial pattern is shown in Figure 14a. This figure shows the changes in the location and intensity of the Aleutian Low and subtropical high that occur during the Fall and Spring. This pattern is modulated in time by the time series shown in Fig. 14b. Unlike the other modes, mode two is dominated by the semi-annual period as shown by the spectrum in Figure 14c. From climatology we expect to see intensification of the Aleutian Low in Fall and weakening in Spring. Conversely, we expect to see intensification of the subtropical high in spring and weakening in fall. The diagonal band of negative contours in the spatial pattern for mode one is also present in this mode, but at a decreased intensity and higher frequency modulation. The positive contours near 55° N, 136° W in mode one are also in this mode, but they appear to be of higher intensity and shifted to the east.

The third spatial pattern (Fig. 15a) accounts for 8.25% of the

variance. The higher the mode, the lower the portion of the total variance accounted for by the pattern, the more difficult it becomes to interpret its physical basis. This pattern is modulated by the time series in Figure 15b. The power spectrum (Fig. 15c) shows almost all of the power in the annual frequency. The features of this spatial pattern and their effects are similar to those in modes one and two with slight variations of position, magnitude and frequency.

Although modes four through nine are considered statistically significant by the *Overland and Preisendorfer* [1982] method, they account for less and less of the total variance of the data. The physical basis for these modes is not well understood, therefore, they are not discussed further.

To summarize: Over 40% of the variance in the curl of the COADS pseudo wind stress is accounted for in the first three modes. The dominant (first mode) spatial pattern oscillates primarily on an annual period and establishes a pressure gradient which results in a forced coastal signal seen in the model results.

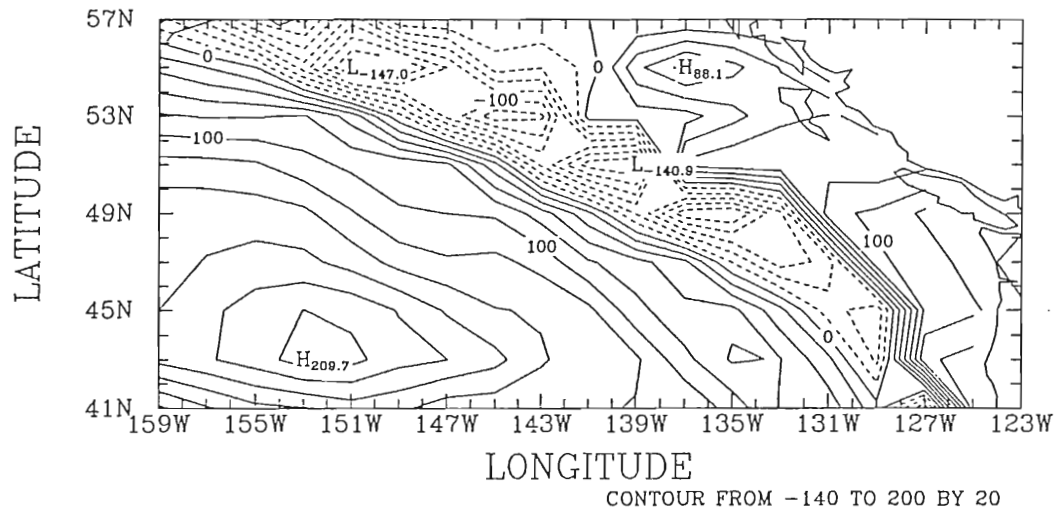


Figure 13a: Contour plot of the spatial pattern for EOF mode one. The high contour in the southwest corner reflects the annual southward migration of the Aleutian Low. The other high contour near 55° N, 136° W is believed to be caused by a low pressure system frequently located there. The diagonal band of negative curl influences the model results forcing an annual signal along the coast.

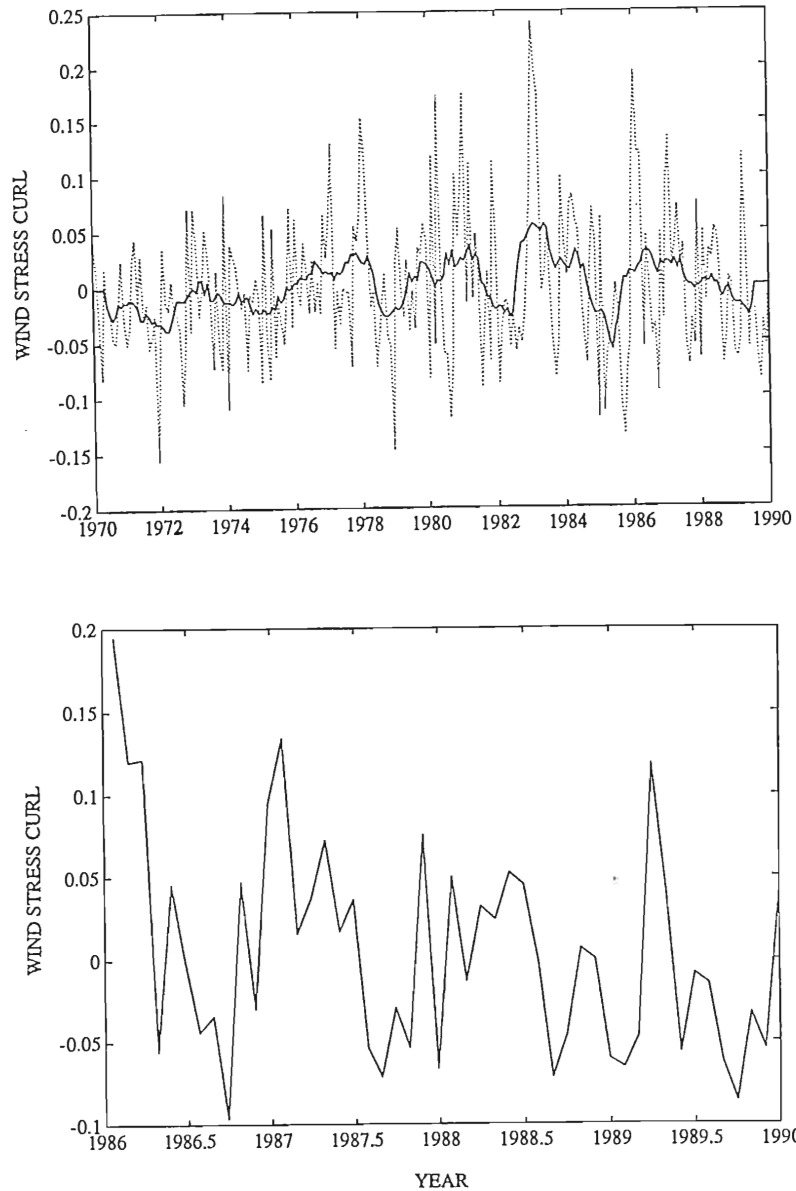


Figure 13b-c: (b) Twenty year time series of EOF mode one with the 12 month running mean superimposed showing the interannual variability. Maxima (minima) normally occurring during winter (summer) months. (c) Detailed plot of the four years of pseudo stress used to force the model. The spatial pattern in Fig. 13a is multiplied by this time series. There is an intensification of the spatial pattern for large positive peaks, little change when the time series is near unity, and the opposite pattern (positive and negative contours reversed) for large negative peaks.

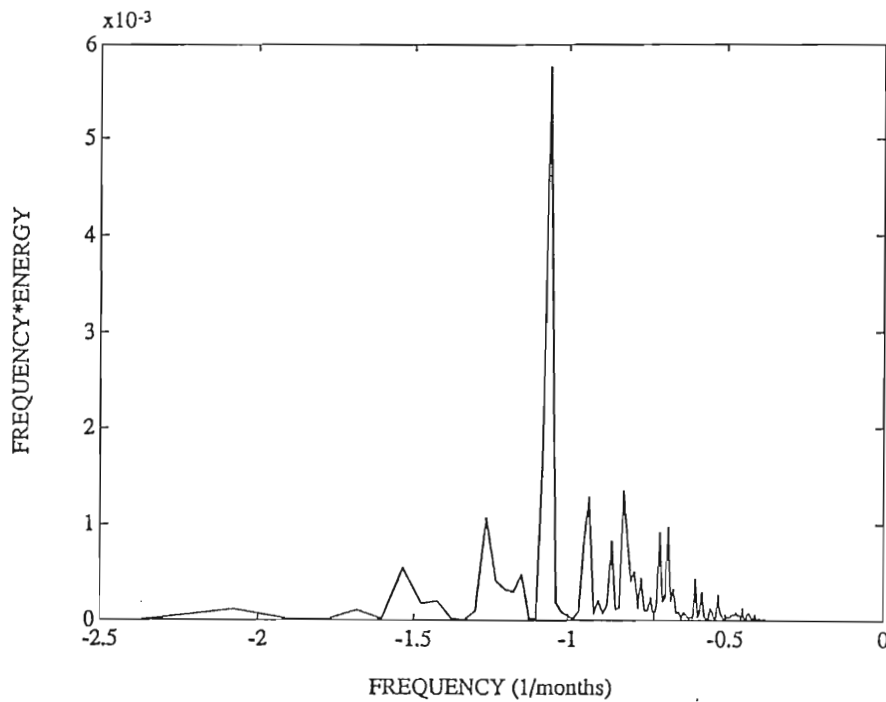


Figure 13d: Power spectrum of EOF mode one. The abscissa units for $\log_{10}(\text{frequency})$ in this and all spectra plots in this section is months^{-1} , and the ordinate units are energy multiplied by frequency. This plot shows that the annual period (spike at -1.1) dominates. There also is some energy at the semi-annual (spike at -0.75) and interannual periods (spike at -1.25). Thus the variations in the spatial pattern in Fig 13a occur predominantly over periods of one year.

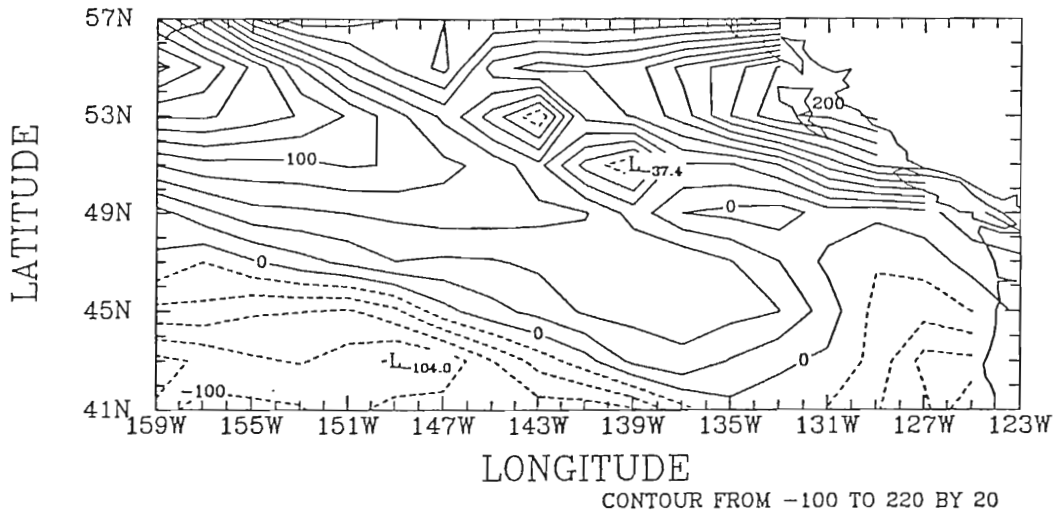


Figure 14a: Contour plot of the spatial pattern for EOF mode two. The negative contours in the lower portion indicate that the intensity of the subtropical high is increased (decreased) when the time series in Fig. 14b is positive (negative). Likewise, the "H" contour in the mean representative of the Aleutian Low is weakened (intensified) and moved northwestward (southeastward) when the time series is positive (negative). This interpretation is supported by climatology. The diagonal band of low contours seen in Fig. 13a is also seen here, but at a much smaller amplitude. The high near 55° N, 136° W in mode one is also present in mode two, but is larger and shifted to the east. The power spectrum for this mode indicates that this pattern's primary period of oscillation is six months.

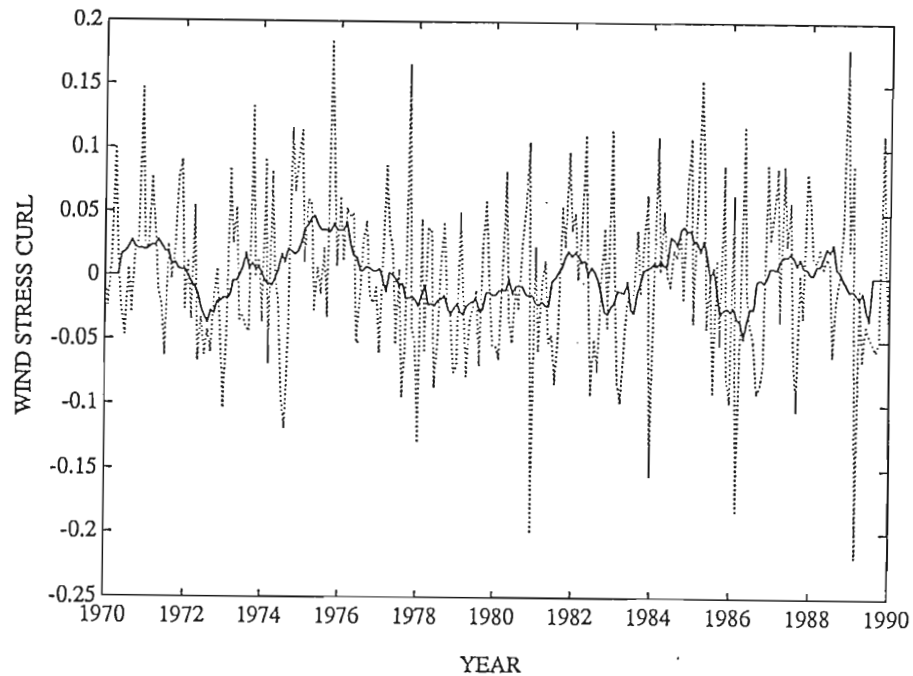


Figure 14b: Time series plot of EOF mode two. The spatial pattern in Fig. 14a is multiplied by this time series, causing intensification for large

Figure 14b: Time series plot of EOF mode two. The spatial pattern in Fig. 14a is multiplied by this time series, causing intensification for large positive peaks, little change when the time series is near unity, and creating the opposite pattern (positive and negative contours reversed) for large negative peaks.

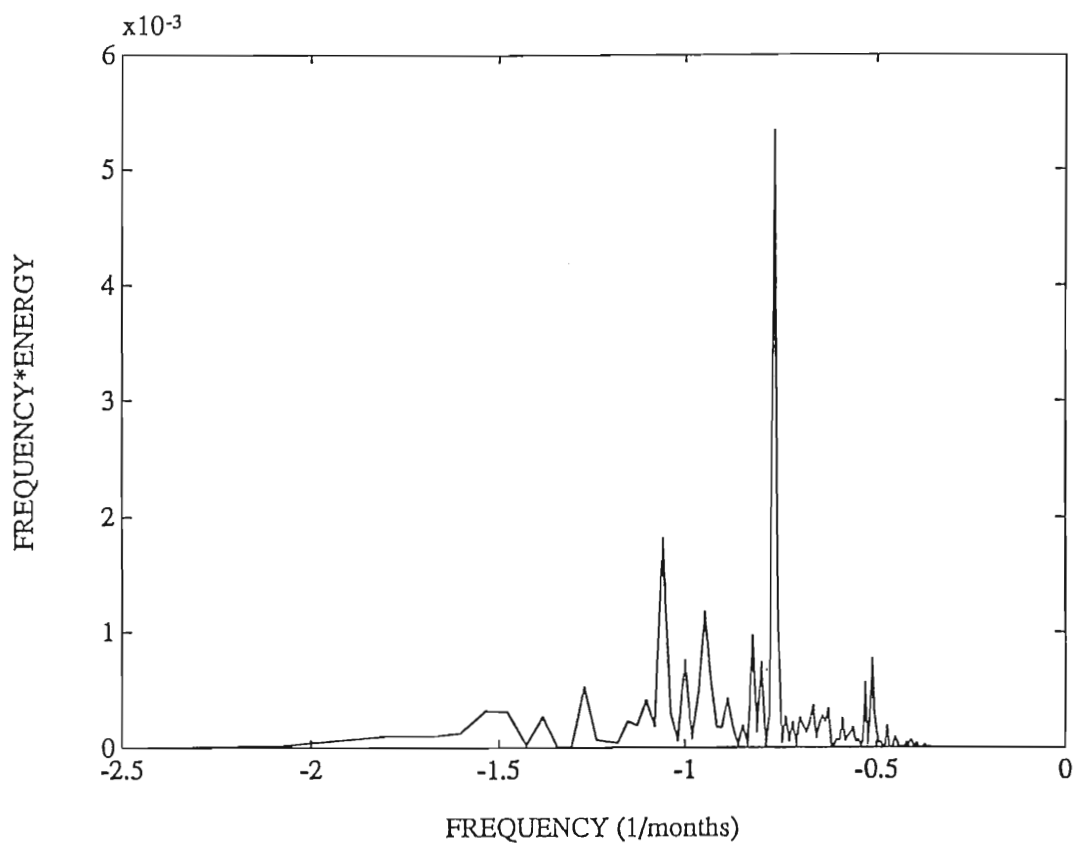


Figure 14c: Power spectrum of EOF mode two. This mode is dominated by the semi-annual period (spike at -0.78) with additional energy at periods of nine months and one year.

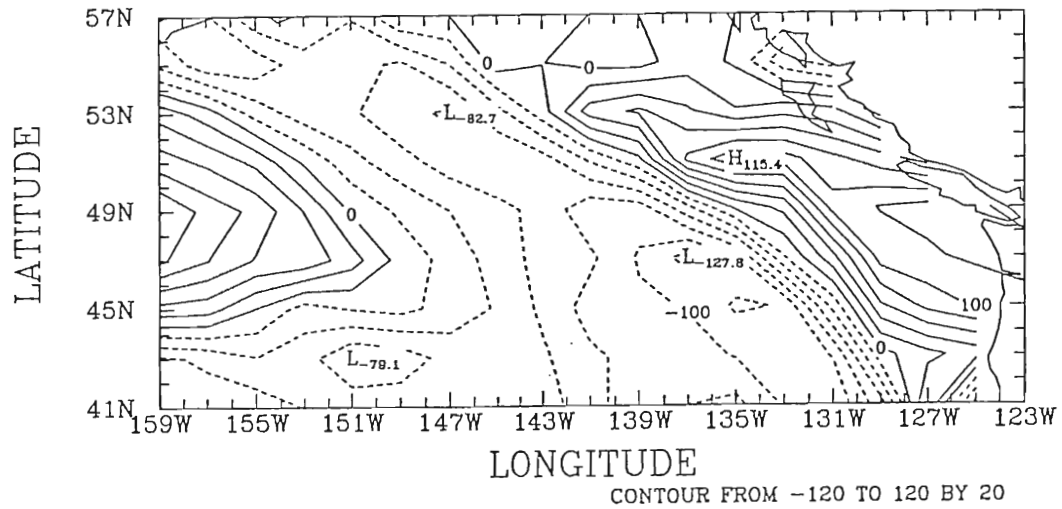


Figure 15a: Contour plot of the spatial pattern for EOF mode three. Patterns and their oscillations are similar to those described in modes one and two.

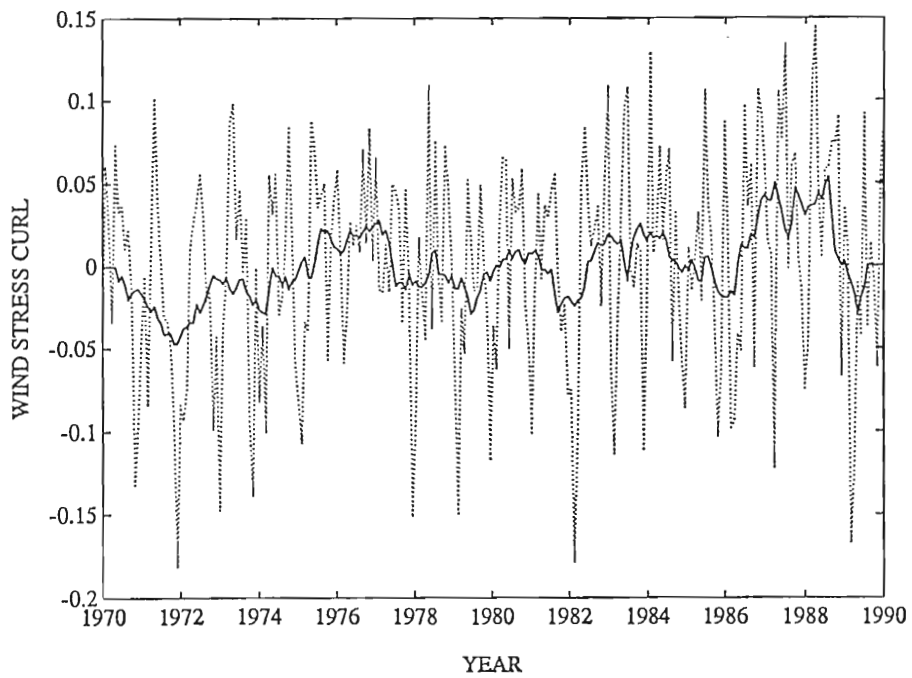


Figure 15b: Time series plot of EOF mode three. The results of the multiplication of the spatial pattern in Fig. 15a with this time series is the same as it was for the previous two modes.

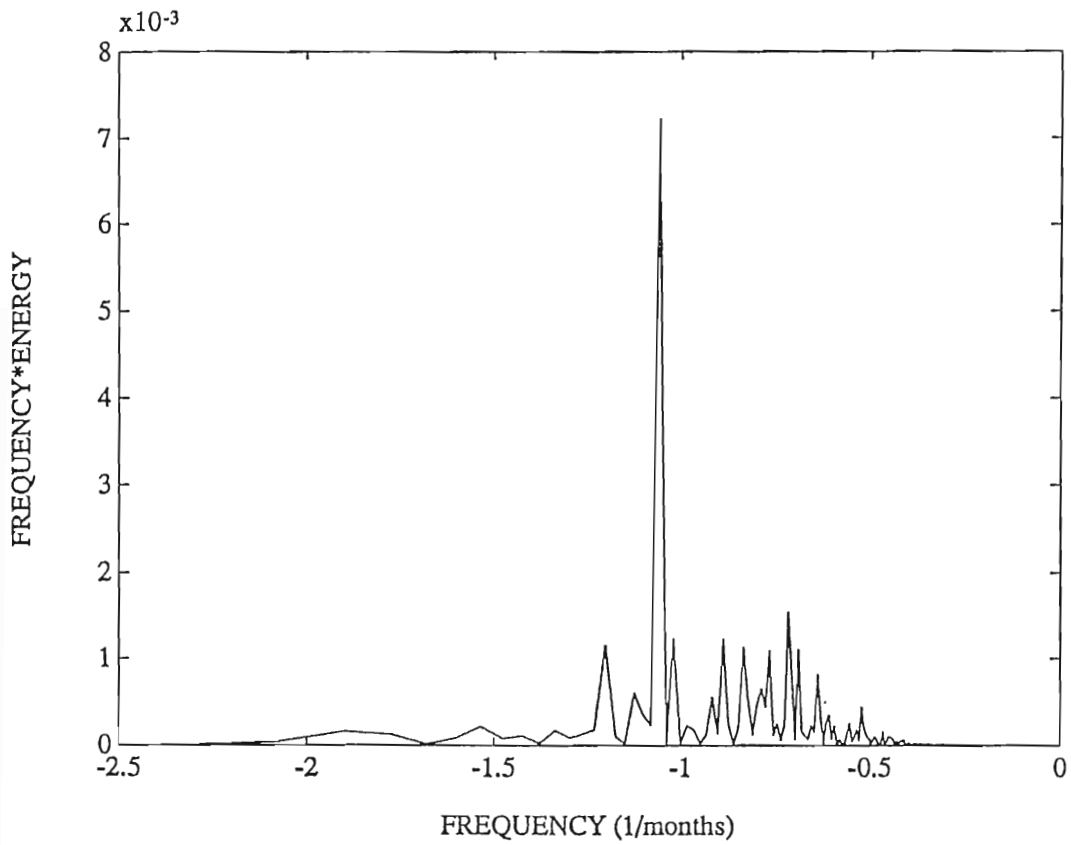


Figure 15c: Power spectrum of EOF mode three. All of the energy is contained in the annual signal.

5. Results

5.1 Model Features

This is the first time a fine resolution, one and a half layer, reduced gravity model has been successfully run at these high latitudes. Figure 16a-c graphically compares the different grid spacing for several popular models. The figure shows the model domain superimposed with various model grid resolutions. The five degree resolution shown in Figure 16a is typical of coupled models, the one degree grid (Fig. 16b) is typical of global circulation models (GCM), and the 1/3 degree resolution shown in Figure 16c is used in WOCE community modelling effort (CME) models (see *Bryan and Holland* [1989] for details of CME models). *Kubota and O'Brien* [1988] use 1/4 degree resolution in their equatorial Pacific Ocean model (not shown) and *Johnson and O'Brien* [1990b] use 1/12th of a degree resolution for their central Pacific model (also not shown). If we were to superimpose the 1/40th of a degree resolution on the domain shown in Figure 16a-c, the coastal outlines would become indistinguishable.

High model resolution is required in order to resolve the regional physics. To resolve the physics properly, one must resolve the internal Rossby deformation radius, which at these latitudes (45° - 60° N) is on the order of 3-11 km. The model resolution of 1/40th of a degree, which is equal to 1.4 km at 60° N, is less than the Rossby radius of deformation and thus enables the model to resolve features of this size adequately.

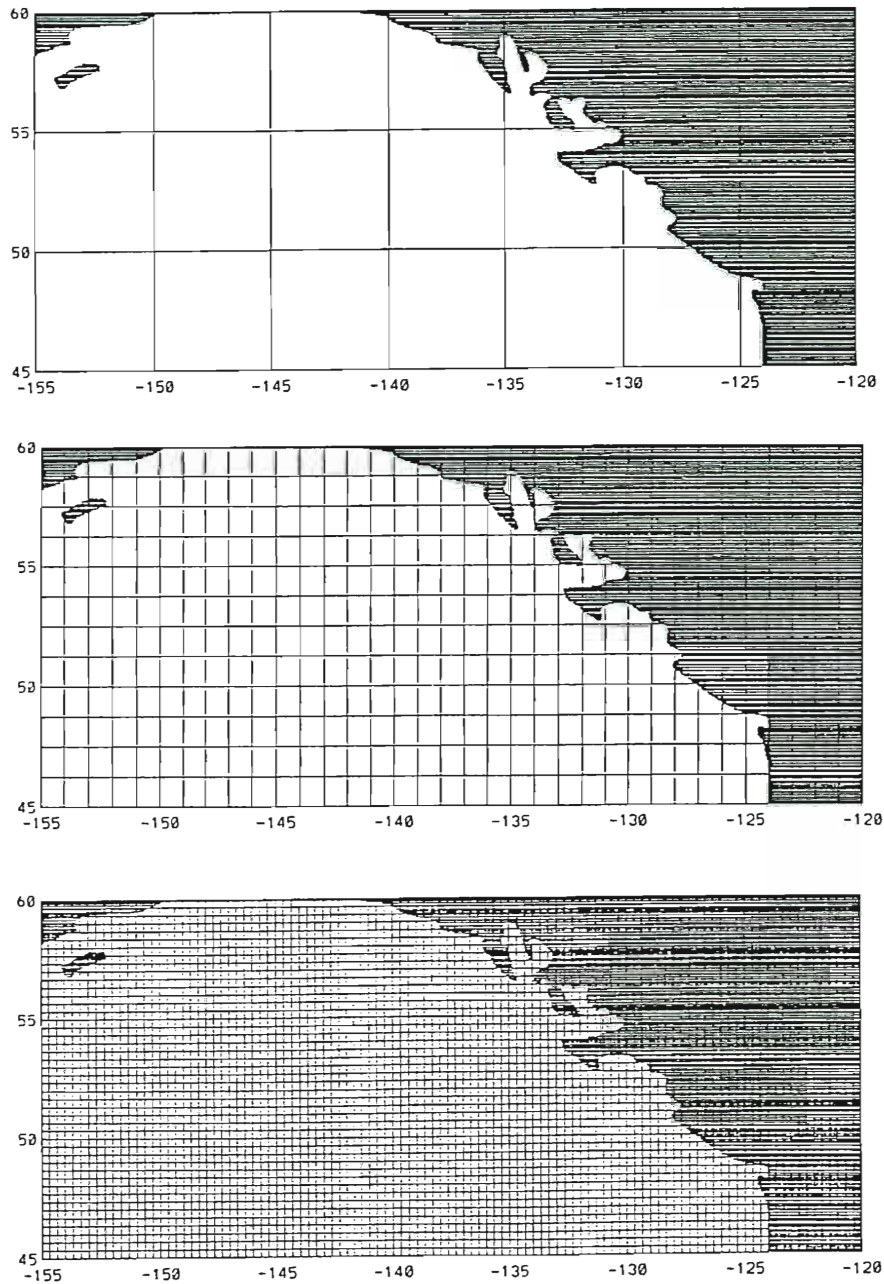


Figure 16a-c: Model domain super imposed with a five degree resolution grid (a), a one degree resolution grid(b), and a 1/3 degree resolution grid.(c)

The high resolution model reproduces the observed upper ocean general circulation in the Gulf of Alaska quite well. An animated color visualization (not shown) of the model results from 1986 through the end of 1989 shows the following features:

The omnipresent Alaskan Gyre is well developed showing seasonal and interannual variability. South of the gyre is the eastward flowing Subarctic Current, bifurcating as it impinges upon the West Coast of North American to form the southward flowing California Current and the northward flowing Alaska Current. The Alaska Current continues to track north and west along the continental slope. The Alaska Current narrows and intensifies south of Kodiak Island and flows southwestward out of the domain completing the gyre. Near 145° W the westward flowing Alaska Current divides, one portion remaining close to the coast, the other merging back into the Alaska Current. The portion remaining near the coast resembles the Alaska Coastal Current (ACC):

The features described in the previous paragraph are shown in Figure 17. The most prominent feature is the well developed Alaskan Gyre centered near 57° N, 147° W. In the lower portion of Figure 17 we see the model representation of the eastward flowing Subarctic Current which splits or bifurcates when it impinges upon the North American Continent. The weak, disorganized flow in the bifurcation region is characteristic of this region (*Royer*, personal communication). The central eastern portion of the model domain shows the northern branch of the bifurcation, more commonly known as the Alaska Current. This shows that the model provides a good simulation of bifurcation regions and of diffuse eastern

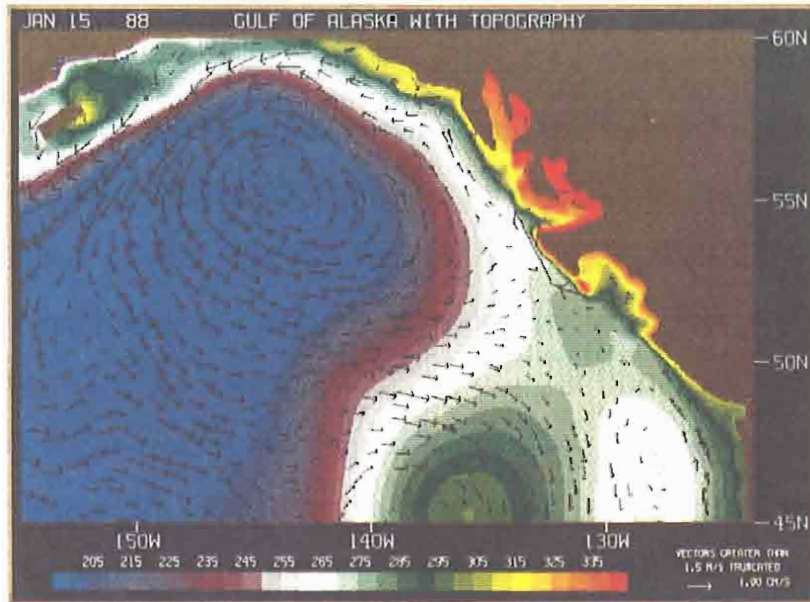


Figure 17: Model solution for 15 JAN 88. The arrows represent surface velocity vectors whose length is proportional to speed which is scaled in relation to the one cm/sec vector in the lower right hand corner. The cross isopycnal flows marked by very small velocity vectors are extremely weak but nevertheless show ageostrophic flow. The colors represent model upper layer thickness (ULT) or depth to the thermocline (in meters) which is an analog of sea surface height. The color bar shows that the reds represent deep ULT (high sea surface height/downwelling region) and the blues represent shallow ULT (low sea surface height/upwelling region). The Alaskan Gyre is seen in the upper left hand portion of the domain contoured from cyan to purple. The eastward flowing Subarctic Current in the southern portion of the figure splits as it impinges on the continental boundary. It flows northward as the Alaska Current and following the coastal geometry bends westward until it flows southwestward past Kodiak Island. The Alaska Current splits near 145° W and a portion of the current hugs the coast similar to the ACC, while the remainder of the current continues flowing west. South of Kodiak the Alaska Current narrows and coastal geometry bends westward until it flows southwestward past Kodiak Island. The Alaska Current splits near 145° W and a portion of the current hugs the coast similar to the ACC, while the remainder of the current continues flowing west. South of Kodiak the Alaska Current narrows and intensifies forming into the Alaskan Stream. This demonstrates the ability of the model to simulate the Alaskan Gyre, bifurcation regions, and eastern and western boundary currents as well.

boundary currents. The Alaska Current continues to flow north along the Canadian and southern Alaskan coasts. In the northern Gulf of Alaska the flow turns westward and eventually flows southwestward south of Kodiak Island and the Alaskan Peninsula. Near 145° W a portion of the Alaska current splits to the north of the main flow hugging the coast in a manner similar to the ACC. The intensification of the flow south of Kodiak is indicative of the formation region of the Alaskan Stream. This result also demonstrates the ability of the model to replicate western boundary currents.

The general model results described in the previous paragraphs display a distinct annual cycle. The wind forced model solution reveals a coastal signal that propagates from 50° N northwestward along the coast beginning in early winter and arriving at Kodiak several months later; suggesting considerable phase difference along the coast. This coastal signal is driven by the model forcing and can be seen in the dominant annual and semi-annual wind stress curl patterns shown earlier in EOF modes one and two which increase in amplitude from southeast to northwest. The model sea level responds first in the southeast, near 50° N, then increases towards the northwest. High sea level initially forms along the Canadian coast during the late fall season as seen in Figure 18a. In about two or three months the sea level all along the coast has increased in amplitude. The high sea level signal in Figure 18a moves northward and covers the entire coast from 50° N to Kodiak Island by February (Figure 18b). The sea level signal begins to fall in early spring (Figure 18c), and by early fall, there is relatively low sea level along the entire coast (Figure 18d).

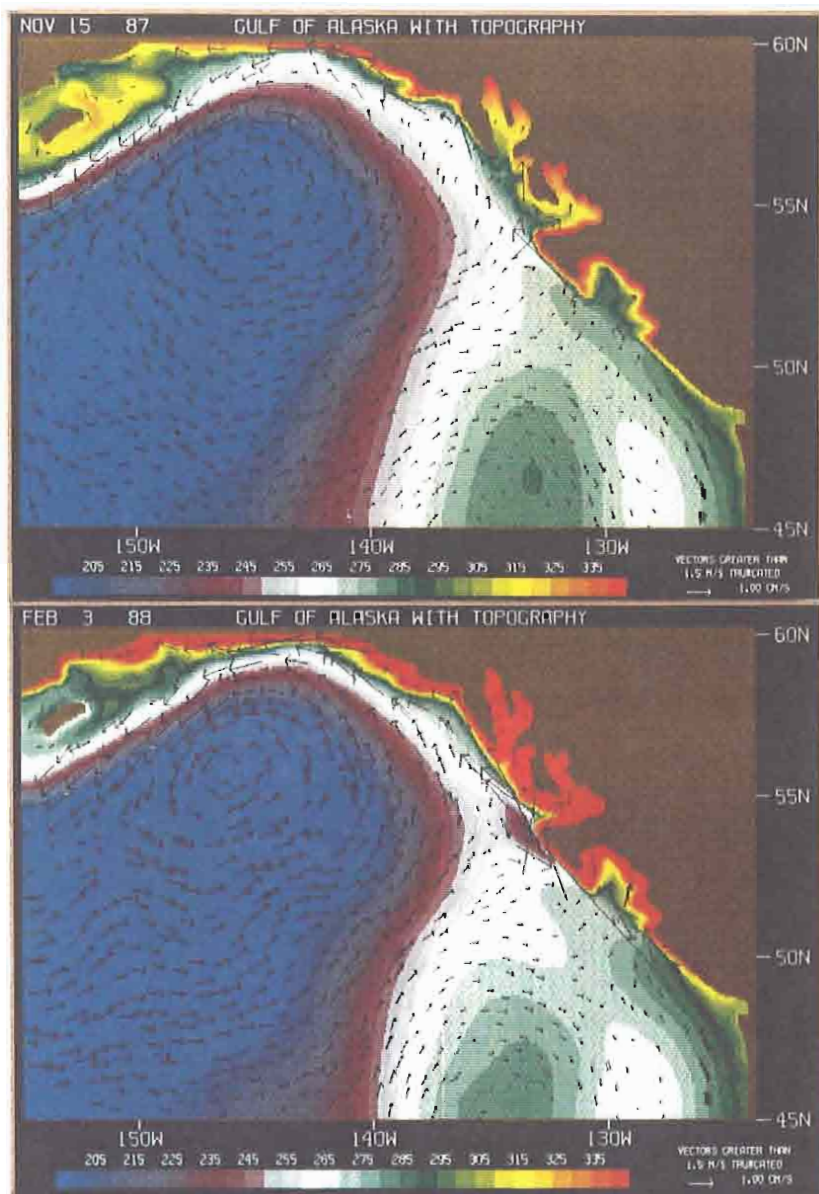
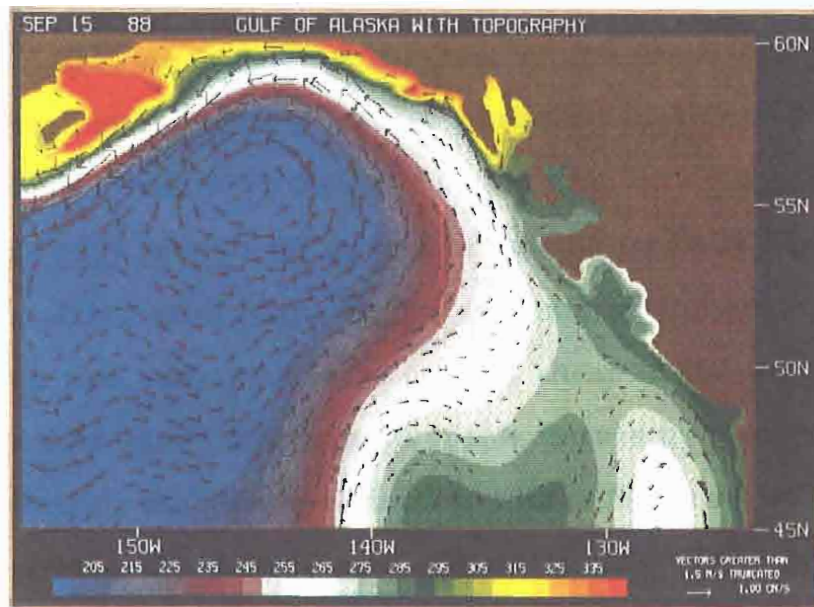
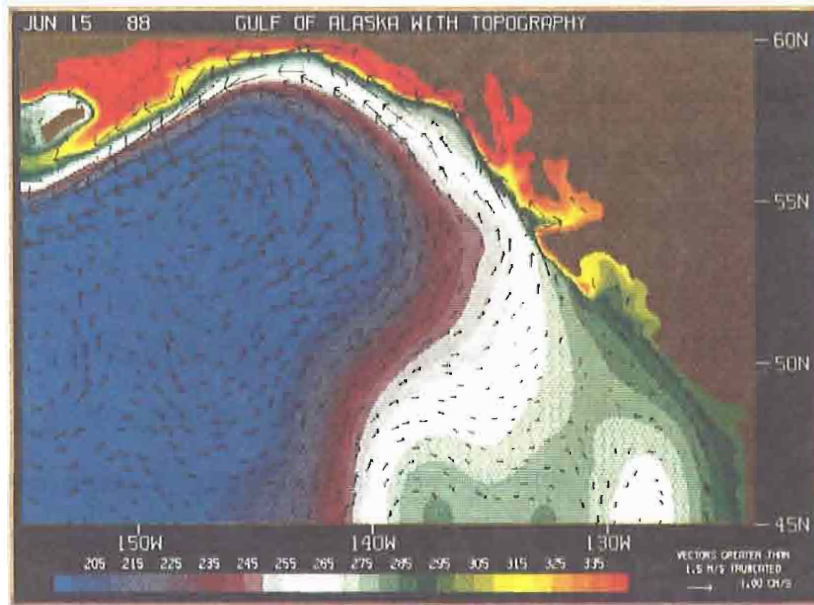


Figure 18a-d: This series of figures shows the seasonal coastal sea level signal of the model results. Figure 18a shows the high coastal sea level (thin red band) beginning to form in November near 53° N. The red band increases in magnitude (thickness) and reaches its northern extent (near Kodiak island) by February 1988 (Fig.18b). The decrease in coastal sea level occurs in the spring, beginning in the southeast and continues to decrease throughout the summer. By mid June, the southern extent of the high sea level signal has moved north from 50° N to north of Queen Charlotte Island (Figure 18c). This trend continues throughout the summer so that by early fall the sea level is lowest all along the coast (Fig. 18d). Also notice the red blocking feature northeast of Kodiak Island in Figure 18d. This feature temporarily disrupts the flow through the Strait during the Fall.



From September to November, a large blocking feature forms northeast of Kodiak temporarily disrupting the flow through Shelikof Strait (Figure 18d). During the remaining months of the year weak flows pass through the Strait. The annual model sea level signal (high (low) sea level in late winter (summer)) is in general agreement with observed annual sea level trends.

In addition to the general model results, there are some specific features generated by the model that warrant further discussion. The model occasionally generates an anticyclonic feature near 58°N , 140°W that resembles the Sitka eddy (Figure 19). This feature can be found in the model solution during all four seasons of the year, and persists for at least two to three months. In contrast with observations of the Sitka eddy by *Tabata* [1982], the model feature is smaller and does not propagate.

Another interesting feature generated by the model is an intense cyclonic eddy feature northwest of Queen Charlotte Island shown in Figure 20. This eddy persists for up to four months typically forming in January and remaining until May. Strong currents on the order of 10-15 cm/sec surround this eddy with large current shear to the west. Figure 21a-b shows a decrease in the strength of this feature from one year to the next, demonstrating the annual variability within the model solution. While we are exploring the driving mechanisms of this eddy, the model physics dictate that it cannot be due to baroclinic instabilities, nor any thermodynamic processes. Rather, it must be a result of the wind forced solution, possibly modified by topographic effects as the fluid tries to conserve its potential vorticity. This feature has not yet been reported in the

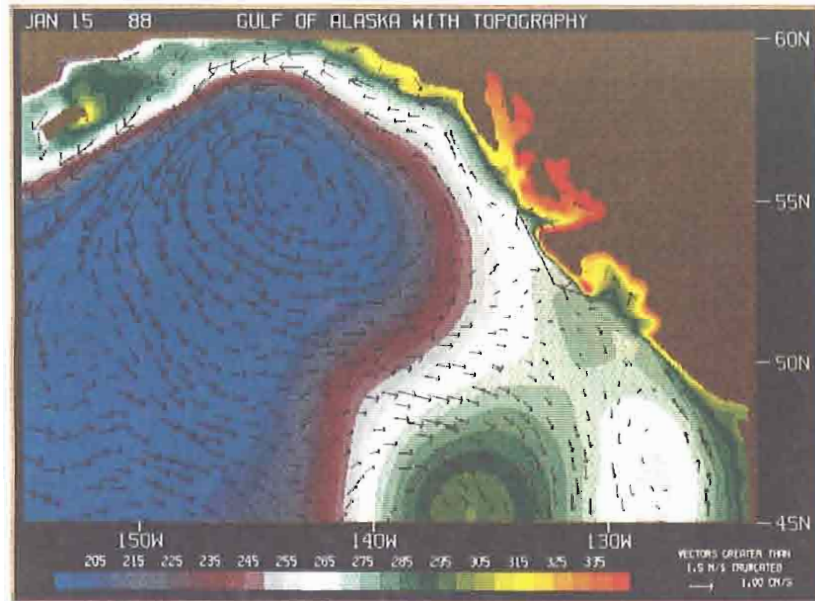


Figure 19: Model solution for January 15, 1988 showing the anticyclonic feature near 58° N, 136° W, which is similar to the Sitka eddy. It is found at various times throughout the model solution.

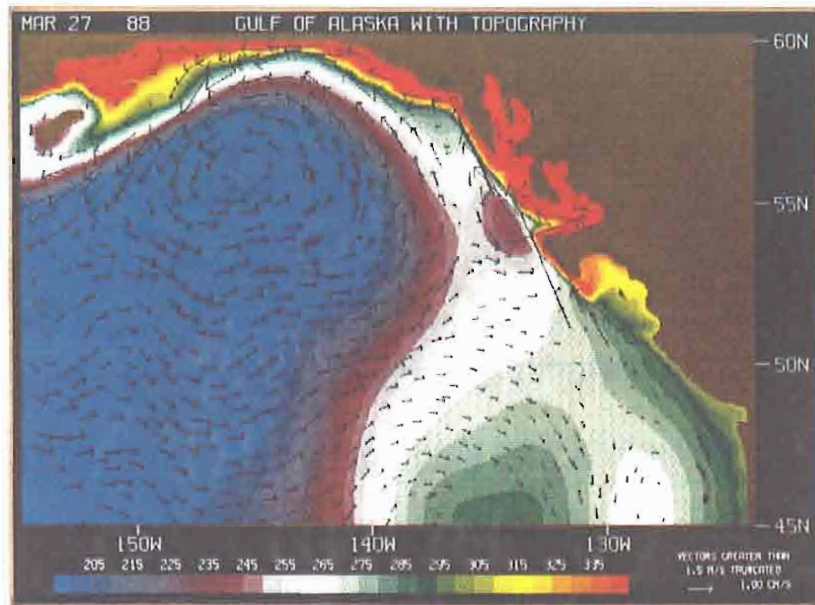
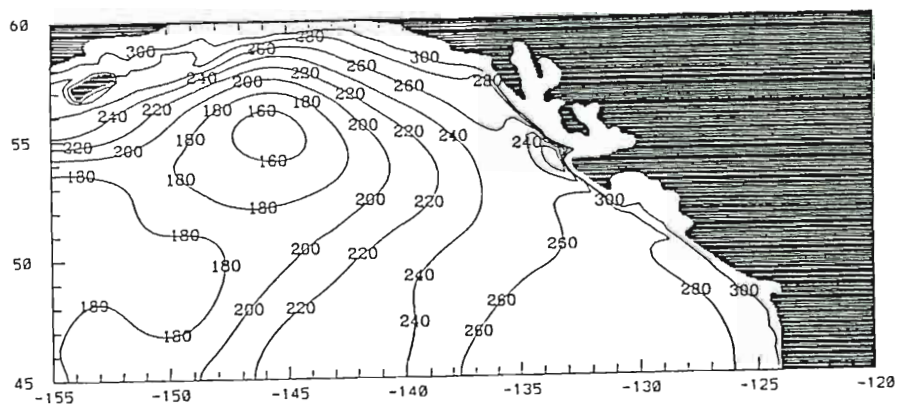


Figure 20: The model generates a cyclonic eddy feature shown by the circular purple contours northwest of Queen Charlotte Island. The eddy

Figure 20: The model generates a cyclonic eddy feature shown by the circular purple contours northwest of Queen Charlotte Island. The eddy forms in January and persists until May. Its formation is believed to be a result of wind forcing and topographic effects in conjunction with potential vorticity conservation.

9/ 2/87

UPPER LAYER THICKNESS



9/ 2/88

UPPER LAYER THICKNESS

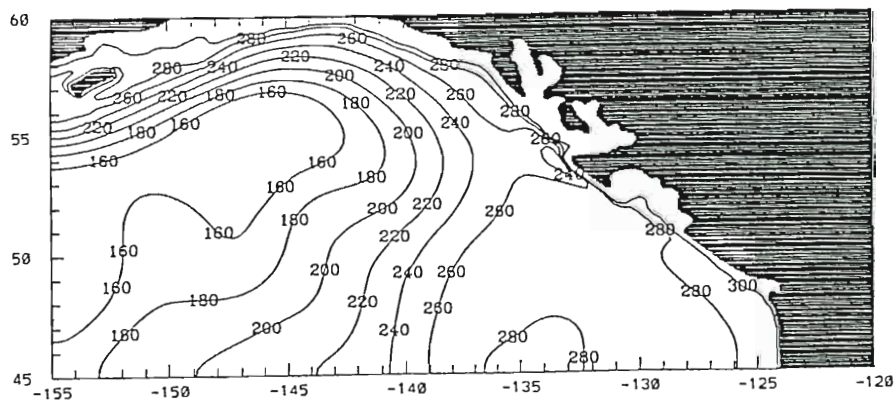


Figure 21a-b: The upper(a) and lower(b) figures show the annual variability of the cyclonic eddy feature northwest of Queen Charlotte Island.

Figure 21a-b: The upper(a) and lower(b) figures show the annual variability of the cyclonic eddy feature northwest of Queen Charlotte Island. There is considerable decrease in the size of the feature (based on contours of ULT shown) from February 9, 1987 to February 9, 1988. This figure demonstrates the interannual variability of the model solution.

literature. When the model is run without bottom topography, these eddy features are not present.

Model volume transports for the first baroclinic mode were computed along 555 km transects south of Cordova, Alaska and southeast of Kodiak Island for 1986 through 1988. Contours of transport (in Sverdrups) integrated over $1/2$ degree intervals are shown in Figure 22. The figure shows the annual variability of the transport near the coast, corresponding to the annual coastal sea level signal shown in Figure 18a-d. Transport values are nearly constant offshore with some eastward transport values at the farthest stations which have crossed the center of the Alaskan Gyre.

The results from model year 1989 (not shown) are quite different compared with the results for 1986-88. All of the features described previously in this section are present in model year 1989, but they are of weaker intensity. These differences can only be attributed to changes in the model forcing function. Examination of the time series for EOF mode one (Fig. 13b) shows that the curl is at its minimum strength during year 1989, so these differences are not unexpected.

5.2 Model Validation

One of the features of reduced gravity baroclinic models is that they tend to replicate the sea surface height (SSH) very well. Comparisons of model "h" fields with monthly mean sea level have been used previously by *Busalacchi et al.* [1983], *Pares-Sierra and O'Brien* [1989] and *Johnson and O'Brien* [1990b] to verify model results.

Initial attempts to verify model results were made by comparing

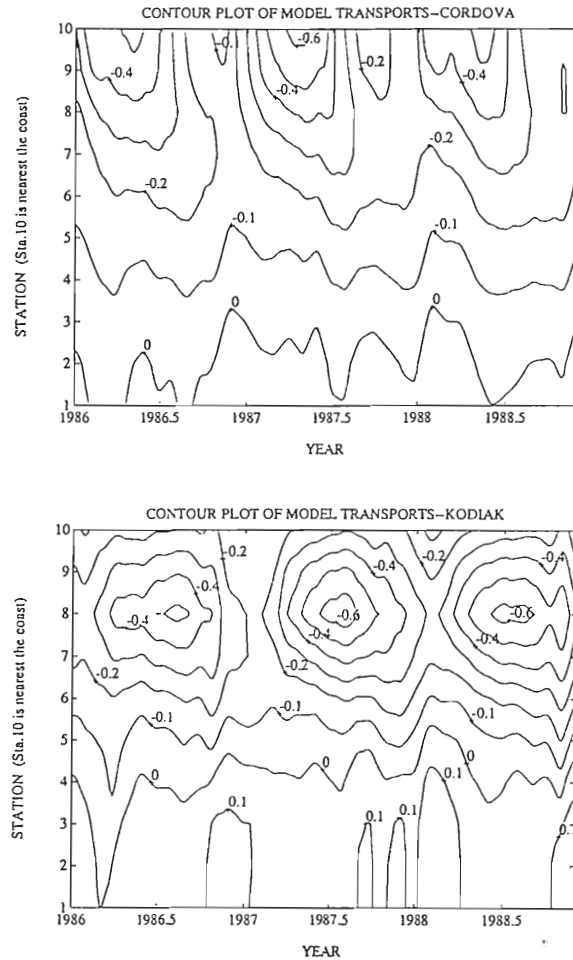


Figure 22: Contours of model transport (in Sverdrups) for 1986 through 1988 integrated over one half degree bands along five degree transects south of Cordova (upper) and southeast of Kodiak (lower). Station ten is nearest the coast so values there represent transport integrated from the coast to one half degree offshore. Negative values indicate westward transport. The values at station nine are transport values integrated over the half degree band between stations ten and nine, and so on for stations further offshore. In the upper figure we see the seasonal variability of the ACC near station ten (nearshore). Transport maxima occur in Spring, minima in Fall, corresponding to the red coastal sea level signal shown in Figure 18a-d. Further offshore (stations 5-1) the transport becomes fairly steady as we approach the interior of the Alaskan Gyre. Southeast of Kodiak (lower figure) we find peak transports occurring in June/July. The concentric contours near stations 9-7 are indicative of the narrowing and intensification of the Alaska Current in this the formation region of the Alaskan Stream. As before we see weakest transports during the Fall. The concentric contours near stations 9-7 are indicative of the narrowing and intensification of the Alaska Current in this the formation region of the Alaskan Stream. As before we see weakest transports during the Fall. Further offshore the flow becomes fairly steady and there is even some eastward transport (indicated by the positive values) as the transect crosses the center of the Alaskan Gyre (stations 3-1).

model "h" field data with monthly mean sea level data obtained from Permanent Service for Mean Sea Level (PSMSL) and National Ocean Service (NOS). These monthly means are computed by simply taking the mean of all of the hourly heights for a given month after removing the tides. A plot of the available monthly mean sea level data (Fig. 23) shows a very coherent signal along the coast.

High frequency information from storms may be aliased into the aforementioned monthly mean sea level data, so we analyzed the hourly NOS sea level data statistically and extract an unaliased monthly mean. Raw power spectra of the hourly data for the years 1986-1989, inclusive at all stations revealed energy in the tidal frequency band (12, 24 hour and fortnightly), seasonal band $\sim O(40-50$ days), semi-annual, annual and interannual bands (see Figure 24a-c). We see very little energy in the four to ten day "storm band", indicating a complex response of the ocean to wind stress. But, because there is still some high frequency information aliased into the monthly mean, we filtered the hourly data using a 10th order, low pass (20 day cutoff) Butterworth Filter, using a 5% cosine taper on both ends to reduce start-up transients. We then sub-sampled the filtered hourly data and obtained a monthly mean which we believe is a better monthly mean value because aliasing is reduced.

Model validation is accomplished by making comparisons of model ULT with filtered hourly NOS sea level data shown in Figure 25a-c. Figure 25a shows exceptionally good agreement between the NOS data and the model "h" field at Neah Bay which is in the southeastern portion of the model domain. This agreement breaks down north of Neah Bay along the

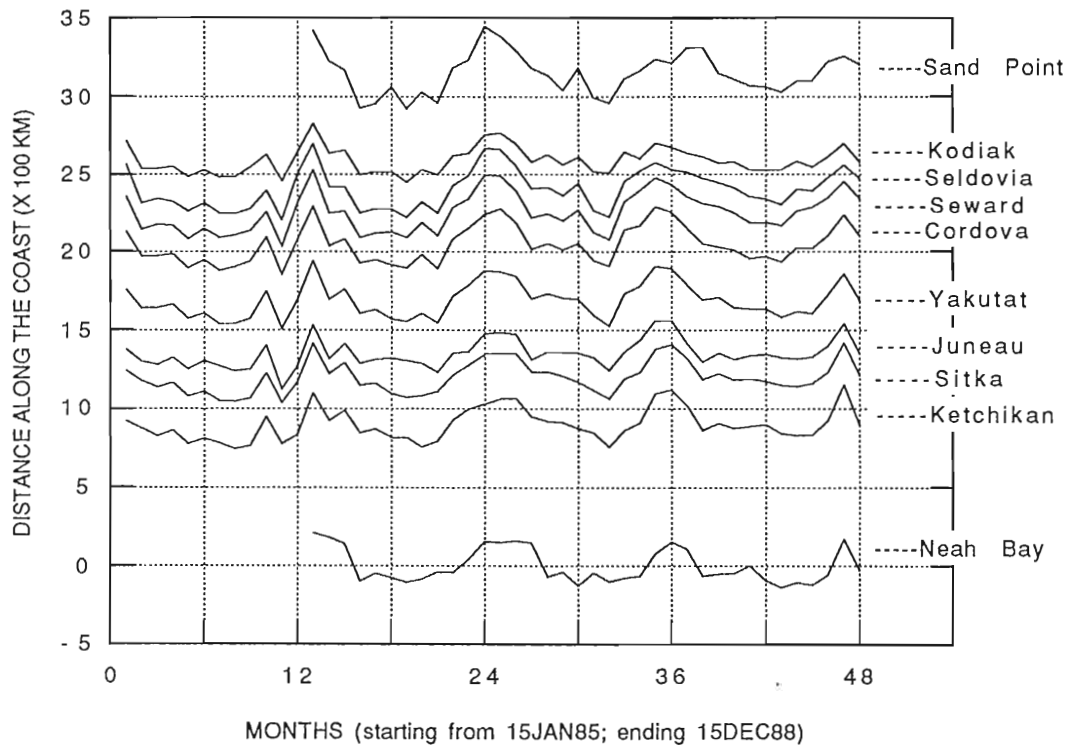


Figure 23: Monthly mean sea level data obtained from PSMSL and NOS. The plots are scaled so that distance along the coast, vice amplitude is

Figure 23: Monthly mean sea level data obtained from PSMSL and NOS. The plots are scaled so that distance along the coast, vice amplitude is plotted on the y axis. All of the sea level stations are in phase showing no propagating features along the coast. Note that the annual peaks shift back 15-30 days per year.

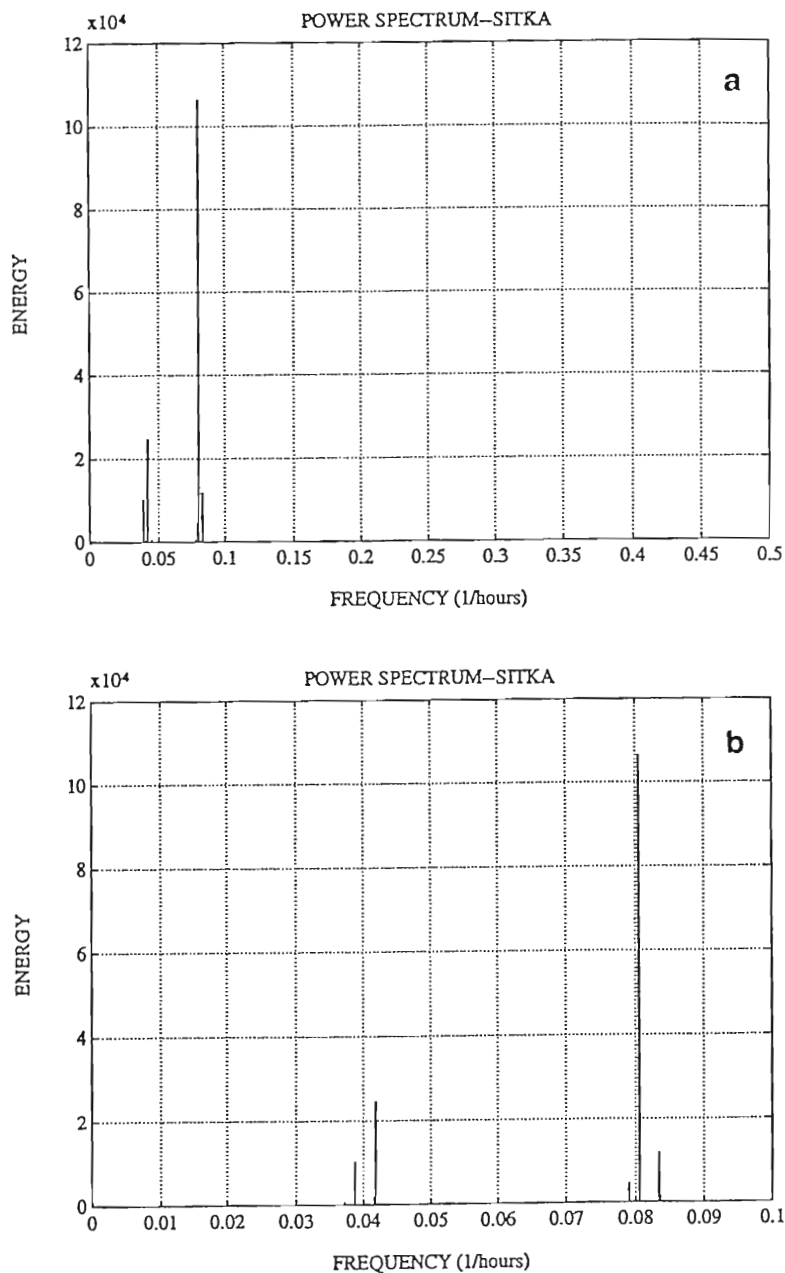
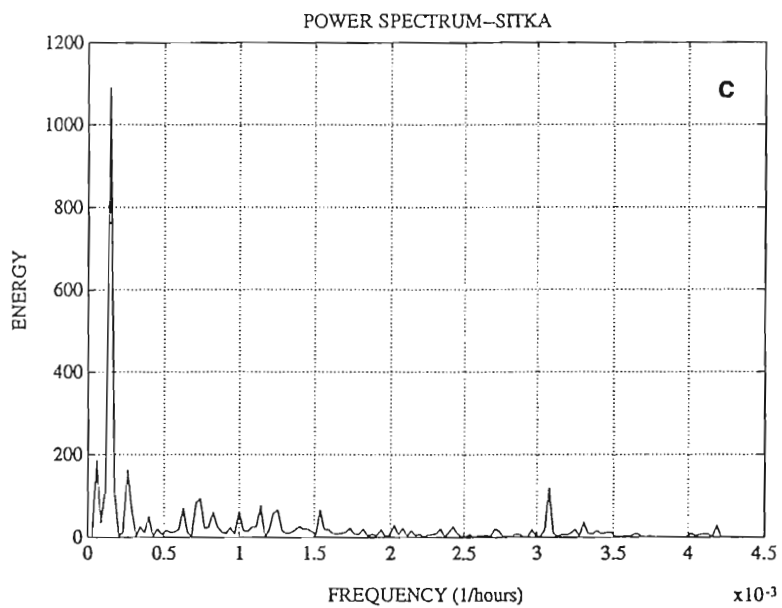


Figure 24a-c: Raw power spectra of hourly NOS sea level data. The majority of the energy lies in the diurnal and semi-diurnal frequency bands (spikes at 0.0805 and 0.041). Additional energy is contained in the annual signal (spike at 0.2×10^{-3}) and fortnightly tides (spike at 3.1×10^{-3}). Little energy was found at the "storm band" frequencies of four to ten days. The (spikes at 0.0805 and 0.041). Additional energy is contained in the annual signal (spike at 0.2×10^{-3}) and fortnightly tides (spike at 3.1×10^{-3}). Little energy was found at the "storm band" frequencies of four to ten days. The scale of the abscissa is changed to allow the reader to examine details of the spectra. Other stations yielded similar spectra, Sitka chosen for example only.



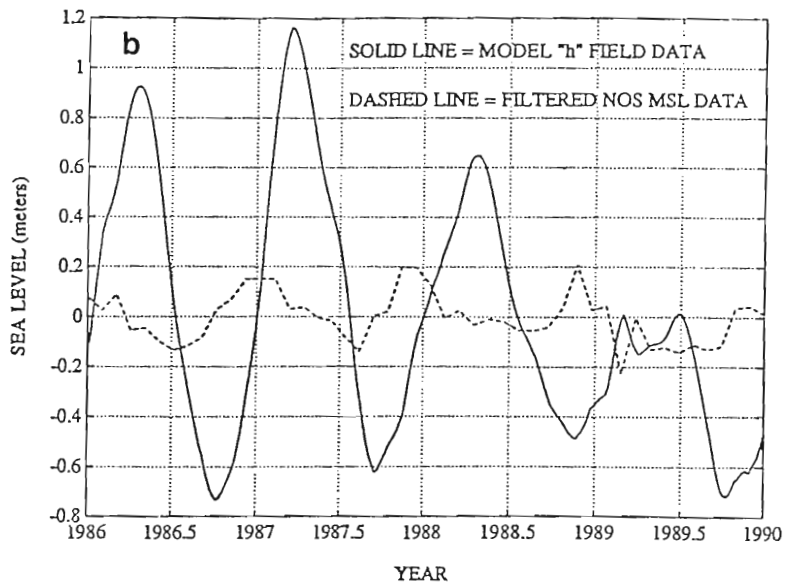
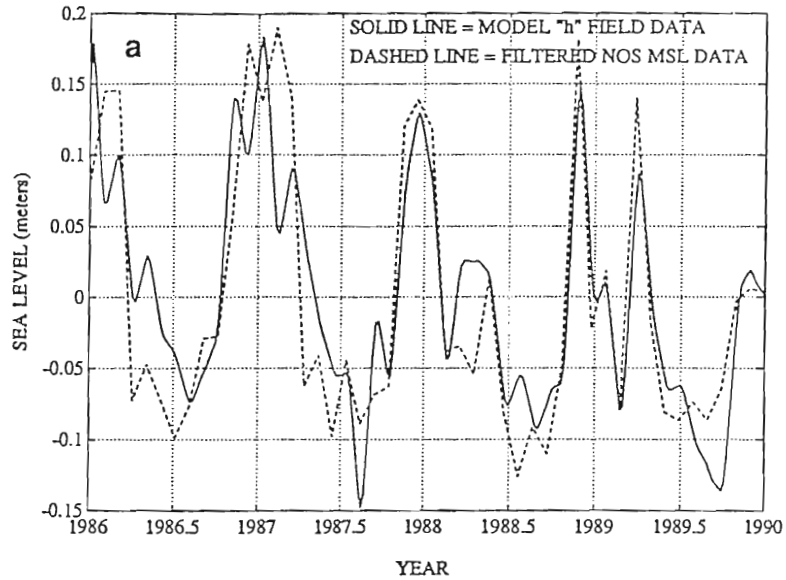


Figure 25a-b: Comparison plots of filtered NOS MSL versus model "h" field data. The southeastern most station, Neah Bay, agrees exceptionally well with the model (a). At Sitka, however, there is poor agreement in amplitude and phase (b).

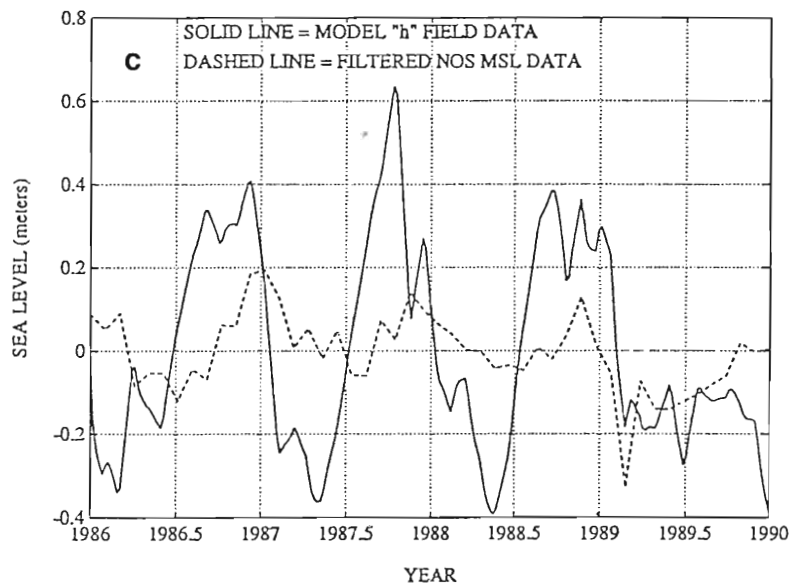


Figure 25c: This figure shows improved agreement at Kodiak, but it is still not as good as Neah Bay.

irregular Alaskan coast. It is poorest at Sitka (Fig.25b) where there are obvious phase shifts and incongruous amplitudes. In the western portion of the domain (i.e. at Kodiak), the agreement has improved slightly (Fig. 25c). This lack of agreement along with the annual coastal signal discussed earlier contradicts the observed sea level shown in Figure 23. However, the spatial pattern in EOF mode one (discussed in section four) suggests an annual wind stress forcing that establishes a pressure gradient along the coast, forcing the model solution shown in this section. Lack of agreement with mean sea level therefore, may be due to an incomplete understanding of the ocean's response to wind forcing, particularly at high latitudes, and not necessarily due to any model shortcomings.

As stated in section two, *Reed et al.* [1981] and *Brooks and Bane* [1981] were not able to find any obvious correlations between their measured current velocities and weekly mean sea level along the coast. *Reed et al.* [1981] concluded that the effects of velocity fluctuations in deep water over the slope did not seem to be transmitted over the shelf and were not readily apparent at the coast. It may be possible therefore, that we should not expect good agreement between model sea level and observed mean sea level at high latitudes and/or in this particular region.

Model results are also verified through a visual comparison with a four layer, finite depth, 1/8th degree Pacific basin model presently being run at NOARL (*Hurlburt*, personal communication). A visual comparison of a sub-region of the NOARL model domain for 15 January of model year 66 with our model result for the same time of year shows very good agreement

between the two (Figure 26a-b). Both models produce similarly shaped gyres. Convergence of the flow occurs in the same location in both models, near the formation region of the Alaskan Stream.

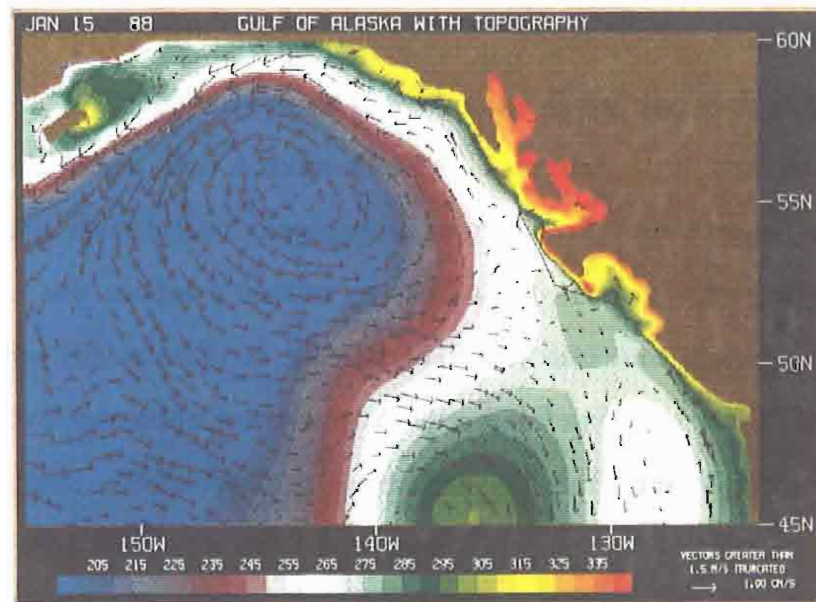
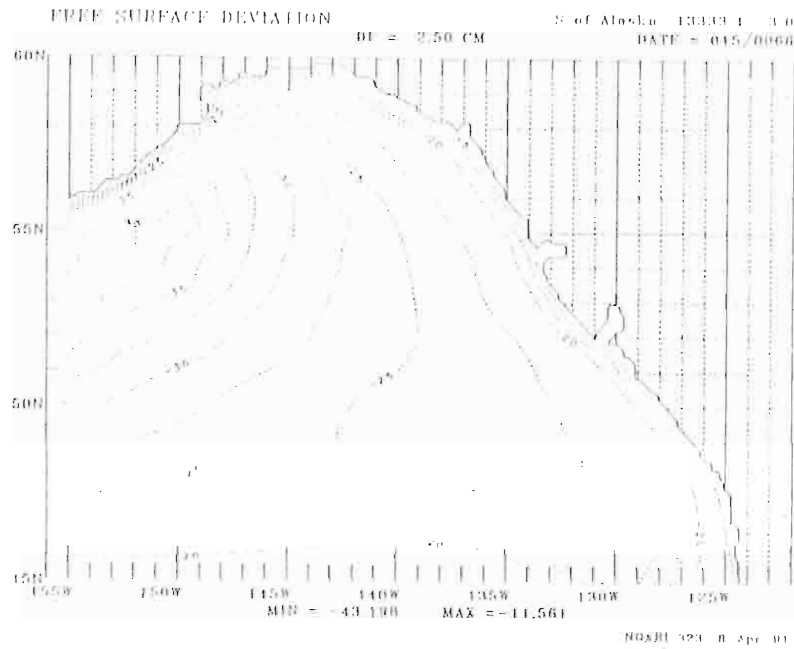


Figure 26a-b: The upper figure shows the free surface deviation for the NOARL Pacific basin model. The NOARL model coastline is plotted as the 200 meter isobath. Both ULT and free surface deviation are analogous to sea surface height. Visual comparison of the model result for the same month (lower figure) with the NOARL model is excellent. The gyres look basically the same with converging contours near 148° W.

6. Conclusions

We have demonstrated that a very high resolution, reduced gravity, baroclinic model simulates many of the observed oceanographic features in the Gulf of Alaska. Qualitative comparisons with other model and observational data are excellent. It is the highest resolution model of its type ever run at these latitudes, testing the limits of applicability for reduced gravity models. We believe that the temporally and spatially coarse winds used to drive the model are the primary reason why the model cannot excite numerous small scale eddies.

However, this model accurately reproduces many of the general features of the region such as the Alaskan Gyre, the Subarctic Current, the Alaska Current, the Alaska Coastal Current, and the Alaskan Stream. The model circulation displays seasonal and interannual variability. In addition, the model solution produces an anticyclonic eddy in the region where the Sitka eddy is known to form, and the model generates an intense cyclonic eddy northwest of Queen Charlotte Island that has yet to be documented. This finding warrants further investigation to determine whether this eddy is a valid feature.

The model evolution (supported by EOF analysis of the wind stress curl) suggests that the wind-forced coastal sea level signal propagates annually along the coast from southeast to northwest, although the data suggests that the wind forced coastal sea level signal propagates annually along the coast from southeast to northwest, although the observed sea level records suggest a signal that is more in phase. Comparison of model results with observed mean sea level is exceptionally

good in some areas and poorer in others. The model shows excellent comparison with a NOARL Pacific basin model. Model verification using GEOSAT altimetry data is currently being studied. Efforts are also being made to extend current work to include remote forcing from coastal Kelvin waves and to increase the frequency of the forcing wind field.

References

- Arakawa, A., Computational design for long-term numerical integration of the equations of fluid motion: two dimensional incompressible flow, Part 1, *J. Comput. Phys.*, **1**, 119-143, 1966.
- Brooks, D.A., and J.M. Bane, Gulf Stream fluctuations and meanders over the Onslow bay upper continental slope, *J. Phys. Oceanogr.*, **11**, 247-256, 1981.
- Bryan, F. O., and W. R. Holland, A high resolution model of the wind- and thermohaline-driven circulation in the north Atlantic Ocean, in *Parameterization of Small-Scale Processes, 'Aha Huliko'a Proceedings*, edited by P. Müller and D. Henderson, University of Hawaii at Manoa, 99-115, 1989.
- Busalacchi, A.J., K. Takeuchi and J.J. O'Brien, Interannual variability of the equatorial Pacific-Revisited, *J. Geophys. Res.*, **88**, 7551-7562, 1983.
- Camerlengo, A.L., and J.J. O'Brien, Open boundary conditions in rotating fluids, *J. Comput. Phys.*, **35**, 12-35, 1980.
- COADS (Comprehensive Ocean-Atmosphere Data Set) Release 1, Users Manual, Climate Research Program, ERL, Boulder, Colorado, 1985.
- Cummins, P.F., and L.A. Mysak, A quasi-geostrophic model of the northeast Pacific. Part I: A preliminary numerical experiment, *J. Phys. Oceanogr.*, **18**, 1261-1286, 1988.
- Cushman-Roisin, B., and J.J. O'Brien, The influence of bottom topography on baroclinic transports, *J. Phys. Oceanogr.*, **13**, 1600-1611, 1983.
- Dodimead, A.J., F. Favorite, and T. Hirano, Review of oceanography of the subarctic Pacific region, *Int. North Pac. Fish. Comm. Bull.*, **13**, 1-195, 1963.
- Dube, S.K., M.E. Luther, and J.J. O'Brien, Documentation of the FSU Indian Ocean model, *Cooperative Indian Ocean modelling project technical report*, Mesoscale air-sea interaction group, The Florida State University, 1986.
- Dube, S.K., M.E. Luther, and J.J. O'Brien, Documentation of the FSU Indian Ocean model, *Cooperative Indian Ocean modelling project technical report*, Mesoscale air-sea interaction group, The Florida State University, 1986.
- Emery, W.J., and K. Hamilton, Atmospheric forcing of interannual variability in the northeast Pacific Ocean, connections with El-Niño,

- J. Geophys. Res.*, **90**, 857-868, 1985.
- Favorite, F., The Alaskan Stream, *Int. North Pac. Fish. Comm. Bull.*, **21**, 1-20, 1967.
- Favorite, F., A.J. Dodimead and K. Nasu, Oceanography of the Subarctic Pacific region, 1960-1971, *Int. North Pac. Fish. Comm. Bull.*, **33**, 187 pp, 1976.
- Hamilton, K., A study of the variability of the return migration route of Fraser River sockeye salmon (*Oncorhynchus nerka*), *Can. J. Zool.*, **63**, 1930-1943, 1985.
- Hamilton, K. and L.A. Mysak, Possible effects of the Sitka eddy on sockeye (*Oncorhynchus nerka*) and pink salmon (*Oncorhynchus gorbuscha*) migration off southeast Alaska, *Can. J. Fish. Aquat. Sci.*, **43**, 498-504, 1986.
- Hardy, D.M., and J.J. Walton, Principal components analysis of vector wind measurements, *J. Appl. Meteorol.*, 1153-1162, 1978.
- Ingraham, W.J., A. Bakum, and F. Favorite, Physical oceanography of the Gulf of Alaska. Final Report, RU-357, Northwest Fisheries Center, National Marine Fisheries Service, Seattle, 132 pp. (Unpublished document).
- Johnson, M.A. and J.J. O'Brien, Modelling the Pacific Ocean, *The International Journal of Supercomputer Applications*, **4:2**, 37-47, 1990a.
- Johnson, M.A. and J.J. O'Brien, The Northeast Pacific Ocean Response to the 1982-1983 El-Niño, *J. Geophys. Res.*, **95**, 7155-7166, 1990b.
- Kubota, M. and J.J. O'Brien, Variability of the upper tropical Pacific Ocean model, *J. Geophys. Res.*, **93**, 13,930-13,940, 1988.
- Legler, D.M., Empirical orthogonal function analysis of wind vectors over the tropical Pacific region, *Bull. Amer. Meteorol. Soc.*, **64**, 234-241, 1983.
- Luther, M.E., and J.J. O'Brien, A model of the seasonal circulation in the Arabian Sea forced by observed winds, *Progress in Oceanography*, **6**, 632-649, 1985.
- Luther, M.E., and J.J. O'Brien, A model of the seasonal circulation in the Arabian Sea forced by observed winds, *Progress in Oceanography*, **6**, 632-649, 1985.
- Mysak, L.A., On the interannual variability of eddies in the northeast Pacific Ocean, *El-Niño North: Niño effects in the eastern subarctic Pacific Ocean*, W.S. Wooster, Ed., University of Washington, Sea

Grant Publication, 97-106, 1985.

- Mysak, L.A., El-Niño, interannual variability and fisheries in the northeast Pacific Ocean, *Can. J. Fish. Aquat. Sci.*, **43**, 464-497, 1986.
- Ohtani, K., Relative transport in the Alaskan Stream in winter, *J. Oceanogr. Soc. Jpn* **26**, 271-182, 1970.
- Overland, J.E., and R.W. Preisendorfer, A significance test for principal components applied to a cyclone climatology, *Mon. Wea. Rev.*, **110**, 1-4, 1982.
- Pares-Sierra, A., and J.J. O'Brien, The seasonal and interannual variability of the California Current system: A numerical model, *J. Geophys. Res.*, **94**, 3159-3180, 1989.
- Reed, R.K., Flow of the Alaskan Stream and its variations, *Deep-Sea Res.*, **31**, 369-386, 1984.
- Reed, R.K., and J.D. Schumacher, Additional current measurements in the Alaskan Stream near Kodiak Island, *J. Phys. Oceanogr.*, **14**, 1239-1246, 1984.
- Reed, R.K., and P.J. Stabeno, Recent observations of variability in the path and vertical structure of the Alaskan Stream, *J. Phys. Oceanogr.*, **19**, 1634-1642, 1989.
- Reed, R.K., and N.E. Taylor, Some measurements of the Alaskan Stream with parachute drogues, *Deep-Sea Res.*, **12**, 777-784, 1965.
- Reed, R.K., R.D. Muench, and J.D. Schumacher, On the baroclinic transport of the Alaskan Stream near Kodiak Island, *Deep-Sea Res.*, **27**, 509-523, 1980.
- Reed, R.K., J.D. Schumacher and J.P. Blaha, Eulerian measurements in the Alaskan Stream near Kodiak Island, *J. Phys. Oceanogr.*, **11**, 1591-1595, 1981.
- Røed, L.P., and O.M. Smedstad, Open boundary conditions for forced waves in a rotating fluid, *SIAM J. Sci. Stat. Comput.*, **5**, 414-426, 1984.
- Royer, T.C., Baroclinic transports in the Gulf of Alaska Part I: Seasonal variations of the Alaska Current, *J. Mar. Res.*, **39**, 239-250, 1981.
- Royer, T.C., Baroclinic transports in the Gulf of Alaska Part I: Seasonal variations of the Alaska Current, *J. Mar. Res.*, **39**, 239-250, 1981.
- Royer, T.C., and W.J. Emery, Circulation in the Gulf of Alaska, *Deep-Sea Res.*, **34**, 1361-1377, 1987.

- Royer, T.C., J.A. Vermersch, T.J. Weingartner, H.J. Niebauer, and R.D. Muench, Ocean circulation influencing the Exxon Valdez oil spill, *Oceanography*, **3**, 3-10, 1990.
- Swaters, G.E., and L.A. Mysak, Topographically induced baroclinic eddies near a coastline, with application to the northeast Pacific, *J. Phys. Oceanogr.*, **15**, 1470-1485, 1985
- Tabata, S., Evidence of a westward-flowing 'Subarctic Countercurrent' in the North Pacific Ocean, *J. Fish. Res. Board Can.*, **33**, 2169, 1976.
- Tabata, S., The anticyclonic baroclinic eddy off Sitka, Alaska in the northeast Pacific, *J. Phys. Oceanogr.*, **12**, 1260-1282, 1982.
- Warren, B.A., and W.B. Owens, Deep currents in the central subarctic Pacific Ocean, *J. Phys. Oceanogr.*, **18**, 529-551, 1988.
- Willmott, A.J., and L.A. Mysak, Atmospherically forced eddies in the northeast Pacific, *J. Phys. Oceanogr.*, **10**, 1769-1791, 1980.

Biographical Sketch

Paul Heim was born in Long Island, N.Y. on December 23, 1960, and grew up in the town of Seaford, N.Y. He graduated valedictorian from Seaford High School in June 1979. He graduated with distinction from the United States Naval Academy on May 25, 1983, receiving a B.S. degree in Oceanography. Upon graduation, he was commissioned an Ensign in the United States Navy, entered flight training in Pensacola, Florida, and was designated a Naval Flight Officer in September 1984. He spent nearly four years flying training and operational missions, including three overseas deployments, with Patrol Squadron Nine, stationed at NAS Moffett Field, California. While attached to Patrol Squadron Nine he was designated a Tactical Coordinator and Mission Commander. His military awards include a Navy Achievement Medal, National Defense Medal, and an Armed Forces Expeditionary Medal. In 1989 he was awarded a NASA scholarship to study Physical Oceanography at the Florida State University in Tallahassee, Florida. He received his M.S. degree in Physical Oceanography in 1991.